The JCMT BISTRO Survey: Studying the Complex Magnetic Field of L43

The Astrophysical Journal, 952:29 (18pp), 2023 July 20 https://doi.org/10.3847/1538-4357/acd6f2

The JCMT BISTRO Survey: Studying the Complex Magnetic Field of L43

Janik Karoly[1], Derek Ward-Thompson[1], Kate Pattle[2], David Berry[3], Anthony Whitworth[4], Jason Kirk[1], Pierre Bastien[5], Tao-Chung Ching[6], Simon Coudé[7,8], Jihye Hwang[9,10], Woojin Kwon[11,12], Archana Soam[13], Jia-Wei Wang[14], Tetsuo Hasegawa[15], Shih-Ping Lai[14,16], Keping Qiu[17,18], Doris Arzoumanian[19], Tyler L. Bourke[20,21], Do-Young Byun[9,10], Huei-Ru Vivien Chen[14,16], Wen Ping Chen[22], Mike Chen[23], Zhiwei Chen[24], Jungyeon Cho[25], Minho Choi[9], Youngwoo Choi[26], Yunhee Choi[9], Antonio Chrysostomou[20], Eun Jung Chung[25], Sophia Dai[27], Victor Debattista[1], James Di Francesco[23,28], Pham Ngoc Diep[29], Yasuo Doi[30], Hao-Yuan Duan[16], Yan Duan[27], Chakali Eswaraiah[31], Lapo Fanciullo[32], Jason Fiege[33], Laura M. Fissel[34], Erica Franzmann[33], Per Friberg[3], Rachel Friesen[35], Gary Fuller[21], Ray Furuya[36], Tim Gledhill[37], Sarah Graves[3], Jane Greaves[4], Matt Griffin[4], Qilao Gu[38], Ilseung Han[9,10], Thiem Hoang[9,10], Martin Houde[39], Charles L. H. Hull[40,41,100], Tsuyoshi Inoue[42], Shu-ichiro Inutsuka[43], Kazunari Iwasaki[44], Il-Gyo Jeong[9,45], Doug Johnstone[23,28], Vera Könyves[1], Ji-hyun Kang[9], Miju Kang[9], Akimasa Kataoka[46], Koji Kawabata[47,48,49], Francisca Kemper[50,51,52], Jongsoo Kim[9,10], Shinyoung Kim[9], Gwanjeong Kim[53], Kyoung Hee Kim[9], Mi-Ryang Kim[54], Kee-Tae Kim[9,10], Hyosung Kim[11], Florian Kirchschlager[55], Masato I. N. Kobayashi[19], Patrick M. Koch[14], Takayoshi Kusune[56], Jungmi Kwon[57], Kevin Lacaille[58,59], Chi-Yan Law[60,61], Chang Won Lee[9,10], Hyeseung Lee[25], Yong-Hee Lee[3,62], Chin-Fei Lee[14], Jeong-Eun Lee[54], Sang-Sung Lee[9,10], Dalei Li[63], Di Li[64], Guangxing Li[65], Hua-bai Li[60], Sheng-Jun Lin[16], Hong-Li Liu[65], Tie Liu[66], Sheng-Yuan Liu[14], Junhao Liu[3], Steven Longmore[67], Xing Lu[38], A-Ran Lyo[9], Steve Mairs[3], Masafumi Matsumura[68], Brenda Matthews[23,28], Gerald Moriarty-Schieven[28], Tetsuya Nagata[69], Fumitaka Nakamura[46,70], Hiroyuki Nakanishi[71], Nguyen Bich Ngoc[29,72], Nagayoshi Ohashi[14], Takashi Onaka[73,74], Geumsook Park[9], Harriet Parsons[3], Nicolas Peretto[4], Felix Priestley[4], Tae-Soo Pyo[70,75], Lei Qian[64], Ramprasad Rao[14], Jonathan Rawlings[2], Mark Rawlings[3,76], Brendan Retter[4], John Richer[77,78], Andrew Rigby[4], Sarah Sadavoy[34], Hiro Saito[79], Giorgio Savini[80], Masumichi Seta[81], Ekta Sharma[64], Yoshito Shimajiri[82], Hiroko Shinnaga[71], Mehrnoosh Tahani[83], Motohide Tamura[15,57,84], Ya-Wen Tang[14], Xindi Tang[85], Kohji Tomisaka[46], Le Ngoc Tram[86], Yusuke Tsukamoto[71], Serena Viti[87], Hongchi Wang[24], Jintai Wu[17], Jinjin Xie[27], Meng-Zhe Yang[16], Hsi-Wei Yen[14], Hyunju Yoo[25], Jinghua Yuan[27], Hyeong-Sik Yun[88], Tetsuya Zenko[69], Guoyin Zhang[64], Yapeng Zhang[89], Chuan-Peng Zhang[27,64], Jianjun Zhou[63], Lei Zhu[64], Ilse de Looze[87], Philippe André[90], C. Darren Dowell[91], David Eden[92], Stewart Eyres[93], Sam Falle[94], Valentin J. M. Le Gouellec[95], Frédérick Poidevin[96,97], Jean-François Robitaille[98], and Sven van Loo[99]

[1] Jeremiah Horrocks Institute, University of Central Lancashire, Preston PR1 2HE, UK; jkaroly@uclan.ac.uk
[2] Department of Physics and Astronomy, University College London, WC1E 6BT London, UK
[3] East Asian Observatory, 660 N. A'ohōkū Place, University Park, Hilo, HI 96720, USA
[4] School of Physics and Astronomy, Cardiff University, The Parade, Cardiff, CF24 3AA, UK
[5] Centre de recherche en astrophysique du Québec & département de physique, Université de Montréal, C.P. 6128 Succ. Centre-ville, Montréal, QC, H3C 3J7, Canada
[6] National Radio Astronomy Observatory, 1003 Lopezville Road, Socorro, NM 87801, USA
[7] Department of Earth, Environment, and Physics, Worcester State University, Worcester, MA 01602, USA
[8] Center for Astrophysics, Harvard & Smithsonian, 60 Garden Street, Cambridge, MA 02138, USA
[9] Korea Astronomy and Space Science Institute, 776 Daedeokdae-ro, Yuseong-gu, Daejeon 34055, Republic of Korea
[10] University of Science and Technology, Korea, 217 Gajeong-ro, Yuseong-gu, Daejeon 34113, Republic of Korea
[11] Department of Earth Science Education, Seoul National University, 1 Gwanak-ro, Gwanak-gu, Seoul 08826, Republic of Korea
[12] SNU Astronomy Research Center, Seoul National University, 1 Gwanak-ro, Gwanak-gu, Seoul 08826, Republic of Korea
[13] Indian Institute of Astrophysics, II Block, Koramangala, Bengaluru 560034, India
[14] Academia Sinica Institute of Astronomy and Astrophysics, No.1, Sec.4, Roosevelt Road, Taipei 10617, Taiwan
[15] National Astronomical Observatory of Japan, National Institutes of Natural Sciences, Osawa, Mitaka, Tokyo 181-8588, Japan
[16] Institute of Astronomy and Department of Physics, National Tsing Hua University, Hsinchu 30013, Taiwan
[17] School of Astronomy and Space Science, Nanjing University, 163 Xianlin Avenue, Nanjing 210023, People's Republic of China
[18] Key Laboratory of Modern Astronomy and Astrophysics (Nanjing University), Ministry of Education, Nanjing 210023, People's Republic of China
[19] Division of Science, National Astronomical Observatory of Japan, 2-21-1 Osawa, Mitaka, Tokyo 181-8588, Japan
[20] SKA Observatory, Jodrell Bank, Lower Withington, Macclesfield SK11 9FT, UK
[21] Jodrell Bank Centre for Astrophysics, School of Physics and Astronomy, University of Manchester, Oxford Road, Manchester, UK
[22] Institute of Astronomy, National Central University, Zhongli 32001, Taiwan
[23] Department of Physics and Astronomy, University of Victoria, Victoria, BC V8W 2Y2, Canada
[24] Purple Mountain Observatory, Chinese Academy of Sciences, 2 West Beijing Road, 210008 Nanjing, People's Republic of China
[25] Department of Astronomy and Space Science, Chungnam National University, Daejeon 34134, Republic of Korea
[26] Department of Physics and Astronomy, Seoul National University, Seoul 08826, Republic of Korea
[27] National Astronomical Observatories, Chinese Academy of Sciences, A20 Datun Road, Chaoyang District, Beijing 100012, People's Republic of China
[28] NRC Herzberg Astronomy and Astrophysics, 5071 West Saanich Road, Victoria, BC V9E 2E7, Canada
[29] Vietnam National Space Center, Vietnam Academy of Science and Technology, Hanoi, Vietnam
[30] Department of Earth Science and Astronomy, Graduate School of Arts and Sciences, The University of Tokyo, 3-8-1 Komaba, Meguro, Tokyo 153-8902, Japan
[31] Indian Institute of Science Education and Research (IISER) Tirupati, Rami Reddy Nagar, Karakambadi Road, Mangalam (P.O.), Tirupati 517 507, India
[32] National Chung Hsing University, 145 Xingda Rd., South Dist., Taichung City 402, Taiwan
[33] Department of Physics and Astronomy, The University of Manitoba, Winnipeg, Manitoba R3T2N2, Canada
[34] Department for Physics, Engineering Physics and Astrophysics, Queen's University, Kingston, ON, K7L 3N6, Canada
[35] National Radio Astronomy Observatory, 520 Edgemont Road, Charlottesville, VA 22903, USA
[36] Institute of Liberal Arts and Sciences Tokushima University, Minami Jousanajima-machi 1-1, Tokushima 770-8502, Japan
[37] School of Physics, Astronomy & Mathematics, University of Hertfordshire, College Lane, Hatfield, Hertfordshire AL10 9AB, UK

[38] Shanghai Astronomical Observatory, Chinese Academy of Sciences, 80 Nandan Road, Shanghai 200030, People's Republic of China
[39] Department of Physics and Astronomy, The University of Western Ontario, 1151 Richmond Street, London N6A 3K7, Canada
[40] National Astronomical Observatory of Japan, Alonso de Córdova 3788, Office 61B, Vitacura, Santiago, Chile
[41] Joint ALMA Observatory, Alonso de Córdova 3107, Vitacura, Santiago, Chile
[42] Department of Physics, Konan University, Okamoto 8-9-1, Higashinada-ku, Kobe 658-8501, Japan
[43] Department of Physics, Graduate School of Science, Nagoya University, Furo-cho, Chikusa-ku, Nagoya 464-8602, Japan
[44] Department of Environmental Systems Science, Doshisha University, Tatara, Miyakodani 1-3, Kyotanabe, Kyoto 610-0394, Japan
[45] Department of Astronomy and Atmospheric Sciences, Kyungpook National University, Republic of Korea
[46] Division of Theoretical Astronomy, National Astronomical Observatory of Japan, Mitaka, Tokyo 181-8588, Japan
[47] Hiroshima Astrophysical Science Center, Hiroshima University, Kagamiyama 1-3-1, Higashi-Hiroshima, Hiroshima 739-8526, Japan
[48] Department of Physics, Hiroshima University, Kagamiyama 1-3-1, Higashi-Hiroshima, Hiroshima 739-8526, Japan
[49] Core Research for Energetic Universe, Hiroshima University, Kagamiyama 1-3-1, Higashi-Hiroshima, Hiroshima 739-8526, Japan
[50] Institute of Space Sciences (ICE), CSIC, Can Magrans, E-08193 Cerdanyola del Vallés, Barcelona, Spain
[51] ICREA, Pg. Lluís Companys 23, Barcelona, Spain
[52] Institut d'Estudis Espacials de Catalunya (IEEC), E-08034 Barcelona, Spain
[53] Nobeyama Radio Observatory, National Astronomical Observatory of Japan, National Institutes of Natural Sciences, Nobeyama, Minamimaki, Minamisaku, Nagano 384-1305, Japan
[54] School of Space Research, Kyung Hee University, 1732 Deogyeong-daero, Giheung-gu, Yongin-si, Gyeonggi-do 17104, Republic of Korea
[55] Sterrenkundig Observatorium, Ghent University, Krijgslaan 281-S9, B-9000 Gent, Belgium
[56] Astronomical Institute, Graduate School of Science, Tohoku University, Aoba-ku, Sendai, Miyagi 980-8578, Japan
[57] Department of Astronomy, Graduate School of Science, University of Tokyo, 7-3-1 Hongo, Bunkyo-ku, Tokyo 113-0033, Japan
[58] Department of Physics and Astronomy, McMaster University, Hamilton, ON L8S 4M1, Canada
[59] Department of Physics and Atmospheric Science, Dalhousie University, Halifax B3H 4R2, Canada
[60] Department of Physics, The Chinese University of Hong Kong, Shatin, N.T., Hong Kong
[61] Department of Space, Earth & Environment, Chalmers University of Technology, SE-412 96 Gothenburg, Sweden
[62] School of Space Research, Kyung Hee University, Gyeonggi-do 17104, Republic of Korea
[63] Xinjiang Astronomical Observatory, Chinese Academy of Sciences, Urumqi 830011, Xinjiang, People's Republic of China
[64] CAS Key Laboratory of FAST, National Astronomical Observatories, Chinese Academy of Sciences, People's Republic of China
[65] Department of Astronomy, Yunnan University, Kunming, 650091, People's Republic of China
[66] Key Laboratory for Research in Galaxies and Cosmology, Shanghai Astronomical Observatory, Chinese Academy of Sciences, 80 Nandan Road, Shanghai 200030, People's Republic of China
[67] Astrophysics Research Institute, Liverpool John Moores University, 146 Brownlow Hill, Liverpool L3 5RF, UK
[68] Faculty of Education & Center for Educational Development and Support, Kagawa University, Saiwai-cho 1-1, Takamatsu, Kagawa, 760-8522, Japan
[69] Department of Astronomy, Graduate School of Science, Kyoto University, Sakyo-ku, Kyoto 606-8502, Japan
[70] SOKENDAI (The Graduate University for Advanced Studies), Hayama, Kanagawa 240-0193, Japan
[71] Department of Physics and Astronomy, Graduate School of Science and Engineering, Kagoshima University, 1-21-35 Korimoto, Kagoshima 890-0065, Japan
[72] Graduate University of Science and Technology, Vietnam Academy of Science and Technology, Hanoi, Vietnam
[73] Department of Physics, Faculty of Science and Engineering, Meisei University, 2-1-1 Hodokubo, Hino, Tokyo 191-8506, Japan
[74] Department of Astronomy, Graduate School of Science, The University of Tokyo, 7-3-1 Hongo, Bunkyo-ku, Tokyo 113-0033, Japan
[75] Subaru Telescope, National Astronomical Observatory of Japan, 650 N. A'ohōkū Place, Hilo, HI 96720, USA
[76] Gemini Observatory/NSF's NOIRLab, 670 N. A'ohōkū Place, Hilo, HI 96720, USA
[77] Astrophysics Group, Cavendish Laboratory, J.J. Thomson Avenue, Cambridge CB3 0HE, UK
[78] Kavli Institute for Cosmology, Institute of Astronomy, University of Cambridge, Madingley Road, Cambridge, CB3 0HA, UK
[79] Faculty of Pure and Applied Sciences, University of Tsukuba, 1-1-1 Tennodai, Tsukuba, Ibaraki 305-8577, Japan
[80] OSL, Physics & Astronomy Dept., University College London, WC1E 6BT London, UK
[81] Department of Physics, School of Science and Technology, Kwansei Gakuin University, 2-1 Gakuen, Sanda, Hyogo 669-1337, Japan
[82] Kyushu Kyoritsu University, 1-8, Jiyugaoka, Yahatanishi-ku, Kitakyushu-shi, Fukuoka 807-8585, Japan
[83] Banting and KIPAC Fellowships: Kavli Institute for Particle Astrophysics & Cosmology (KIPAC), Stanford University, Stanford, CA 94305, USA
[84] Astrobiology Center, National Institutes of Natural Sciences, 2-21-1 Osawa, Mitaka, Tokyo 181-8588, Japan
[85] Xinjiang Astronomical Observatory, Chinese Academy of Sciences, 830011 Urumqi, People's Republic of China
[86] University of Science and Technology of Hanoi, Vietnam Academy of Science and Technology, Hanoi, Vietnam
[87] Physics & Astronomy Dept., University College London, WC1E 6BT London, UK
[88] Korea Astronomy and Space Science Institute, Yuseong-gu, Daejeon 34055, Republic of Korea
[89] Department of Astronomy, Beijing Normal University, Beijing100875, People's Republic of China
[90] Laboratoire d'strophysique (AIM), Université Paris-Saclay, Université Paris Cité, CEA, CNRS, AIM, F-91191 Gif-sur-Yvette, France
[91] Jet Propulsion Laboratory, M/S 169-506, 4800 Oak Grove Drive, Pasadena, CA 91109, USA
[92] Armagh Observatory and Planetarium, College Hill, Armagh BT61 9DG, UK
[93] University of South Wales, Pontypridd, CF37 1DL, UK
[94] Department of Applied Mathematics, University of Leeds, Woodhouse Lane, Leeds LS2 9JT, UK
[95] SOFIA Science Center, Universities Space Research Association, NASA Ames Research Center, Moffett Field, CA 94035, USA
[96] Instituto de Astrofisíca de Canarias, E-38200 La Laguna, Tenerife, Canary Islands, Spain
[97] Departamento de Astrofísica, Universidad de La Laguna (ULL), E-38206 La Laguna, Tenerife, Spain
[98] Univ. Grenoble Alpes, CNRS, IPAG, F-38000 Grenoble, France
[99] School of Physics and Astronomy, University of Leeds, Woodhouse Lane, Leeds LS2 9JT, UK
Received 2023 April 27; revised 2023 May 16; accepted 2023 May 17; published 2023 July 14

[100] NAOJ Fellow.

Abstract

We present observations of polarized dust emission at 850 μm from the L43 molecular cloud, which sits in the Ophiuchus cloud complex. The data were taken using SCUBA-2/POL-2 on the James Clerk Maxwell Telescope as a part of the BISTRO large program. L43 is a dense ($N_{H_2} \sim 10^{22}$–10^{23} cm^{-2}) complex molecular cloud with a submillimeter-bright starless core and two protostellar sources. There appears to be an evolutionary gradient along the isolated filament that L43 is embedded within, with the most evolved source closest to the Sco OB2 association. One of the protostars drives a CO outflow that has created a cavity to the southeast. We see a magnetic field that appears to be aligned with the cavity walls of the outflow, suggesting interaction with the outflow. We also find a magnetic field strength of up to $\sim 160 \pm 30$ μG in the main starless core and up to $\sim 90 \pm 40$ μG in the more diffuse, extended region. These field strengths give magnetically super- and subcritical values, respectively, and both are found to be roughly trans-Alfvénic. We also present a new method of data reduction for these denser but fainter objects like starless cores.

Unified Astronomy Thesaurus concepts: Stellar-interstellar interactions (1576); Interstellar magnetic fields (845); Young stellar objects (1834); Dust continuum emission (412); Starlight polarization (1571); Molecular clouds (1072)

1. Introduction

Magnetic fields (*B*-fields) are known to be prevalent throughout the interstellar medium (ISM) and thread through molecular clouds (Planck Collaboration et al. 2016a). Multiple simulations have demonstrated that turbulence and magnetic fields often play a role in the formation of filaments and molecular clouds (Federrath 2015), and although the magnetic field does not appear to dominate as heavily over gravity or turbulence as first thought, it has a nonnegligible influence (Hennebelle & Inutsuka 2019; Krumholz & Federrath 2019).

Most observations of magnetic fields to date have been carried out in nearby, large star-forming regions that may already contain stars or are bright and massive (e.g., Pattle et al. 2017; Soam et al. 2018; Arzoumanian et al. 2021; Kwon et al. 2022). Early observations of dim, prestellar cores were made by Ward-Thompson et al. (2000), but in more recent cases, due to increased sensitivity of polarimeters such as POL-2 on the James Clerk Maxwell Telescope (JCMT), more complex magnetic fields have been observed in molecular clouds where stars have yet to be formed (Liu et al. 2019; Karoly et al. 2020; Pattle et al. 2021). It is important to understand the strength and structure of the magnetic fields in these early stages of star formation since their role may differ from roles played once stars have already formed, for example, due to interaction with stellar feedback (Krumholz & Federrath 2019). Additionally, magnetic fields most likely play a role in forming filamentary structures (Soler et al. 2013), which can then fragment into star-forming regions or individual stars. B fields In STar Forming Regions Observations (BISTRO; Ward-Thompson et al. 2017) is a large program on the JCMT that uses POL-2 to observe the magnetic field in star-forming regions at 850 and 450 μm in order to understand these roles.

Magnetic fields, however, are subject to the influence of numerous processes in molecular clouds. Gravity and turbulence are two factors that can affect the magnetic field structure and strength (Hennebelle & Inutsuka 2019). Additionally, protostellar outflows have been known to either affect, or be affected by, magnetic fields as seen by many instances of the magnetic fields tracing outflows (see Hull et al. 2017, 2020; Lyo et al. 2021; Pattle et al. 2022b).

In this work, we investigate the contribution of the magnetic field to the stability of the starless core within L43. We also investigate the interaction of the magnetic field with the CO outflow of RNO 91, an embedded Class I protostar. This is achieved by using 850 μm polarization observations obtained with the POL-2 polarimeter at the JCMT. The morphology of the plane-of-sky (POS) component of the mean magnetic field (averaged along the line of sight, LOS) in the ISM can be directly inferred from the polarization of dust thermal emission at far-infrared and submillimeter wavelengths (see Andersson et al. 2015, and references therein). Such polarized emission is expected to be perpendicular to the plane-of-sky magnetic field orientation due to the alignment of interstellar dust grains with magnetic fields through radiative alignment torques (RATs; Lazarian & Hoang 2007; Andersson et al. 2015) and (sub) millimeter polarization parallel to the grains' main axis in the Rayleigh regime (Kirchschlager et al. 2019).

This paper is structured as follows: Section 2 is an introduction to the L43 molecular cloud, Section 3 presents the observations and the data reduction process. Section 4 provides a discussion of the main results, such as the dust and outflow properties (Sections 4.1–4.3), the polarization properties (Section 4.4), and the magnetic field morphology and strength (Sections 4.5 and 4.6). Section 5 discusses the relation of magnetic fields with other properties in L43 such as gravity and kinematics (Section 5.1), the alignment of the magnetic field with the outflow (Section 5.2), and how the filament may have evolved over time (Section 5.3). Finally, we summarize the findings of this paper in Section 6.

2. Lynds 43

L43 is a nearby molecular cloud in the northern region of the Ophiuchus star-forming region (see Figure 1) at 120–125 pc, which is the mean distance to the Ophiuchus complex (de Geus et al. 1990; Loinard et al. 2008). As can be seen in Figure 1, L43 is an isolated dense core with a visual extinction >30 mag. It contains a submillimeter-bright starless core (Ward-Thompson et al. 2000) to the east and to the west an embedded young stellar object (YSO), IRAS 16316-1450, a T Tauri star (Herbst & Warner 1981) originally classified as a Class II source currently transitioning from a protostar to a main-sequence star (Andre & Montmerle 1994). However, Chen et al. (2009) and Yoon et al. (2021) have more recently classified it as a Class I source based on Spitzer and spectral line data, respectively. IRAS 16316-1450 is most commonly known as red nebulous object (RNO) 91 (Cohen 1980), although this technically refers to the reflection nebula with which the YSO is associated (Hodapp 1994). The YSO is also

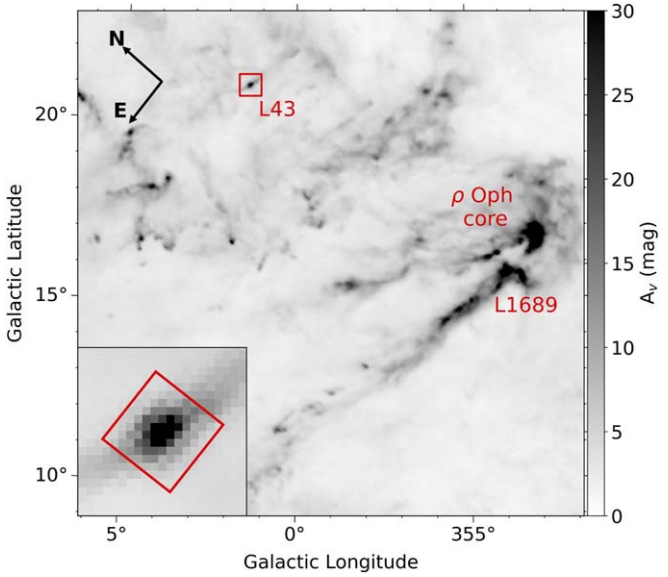

Figure 1. An extinction map of the Ophiuchus region made from Planck dust emission maps (Planck Collaboration et al. 2016b). The inset is a zoomed in picture of the red box labeled L43. The rotated red box in the inset shows the region plotted in Figure 2 in the J2000 coordinate system. The well-known clouds of the ρ Oph core (also known as L1688) and L1689 are labeled as a reference.

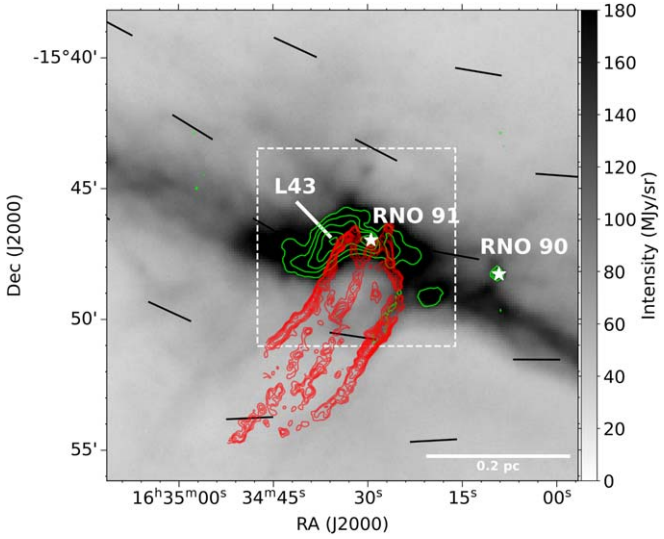

Figure 2. Herschel SPIRE 250 μm dust continuum map with SCUBA-2/POL-2 850 μm dust continuum green contours from this work. Planck *B*-field vectors are overlaid in black and are all normalized to a single length and oversampled at every 5′. The two embedded YSOs are labeled. Additionally, the CO $J = 1$–0 emission from RNO 91 (Lee et al. 2002) is shown in red. The white dashed box shows the area of interest that is plotted in later figures.

associated with an extended, asymmetrical, and bipolar CO outflow (Lee et al. 2002; see also Figure 2) and HCO^+, N_2H^+, and CS emission (Lee & Ho 2005). The CO outflow is detected in the ^{12}CO $J = 1$–0, 2–1 and 3–2 transitions, but there is no detection in the higher transitions (Yang et al. 2018). The CO $J = 1$–0 outflow is shown in Figure 2. The $J = 2$–1 transition is plotted in Figure 1 of Bence et al. (1998). All three of the transitions show a very dominant southern outflow, although the HARP CO $J = 3$–2 data shows a smaller northern lobe as well.

Another YSO, similarly named RNO 90 (Cohen 1980, also known as V1003 Oph) sits farther to the west, ∼0.2 pc away from RNO 91 (see Figure 2), and is also classified as a T Tauri star (Herbst & Warner 1981) but is a much more evolved source, with an age of 2–6 Myr (Garufi et al. 2022) and a protoplanetary disk (e.g., Pontoppidan et al. 2010). It sits at a distance of 114.7–116.7 pc (Bailer-Jones et al. 2018; Gaia Collaboration et al. 2021) suggesting that this star sits either in the foreground of the L43 molecular cloud or perhaps the filament where they are embedded is inclined toward us (assuming the distance to L43 is similar to the mean distance of the larger Ophiuchus region, 120–125 pc). The presence of a reflection nebula for both RNO 90 and 91 suggests they do sit just in front of or are partially embedded in the filament/molecular cloud (Herbst & Warner 1981). L43 is therefore a unique environment that consists of an older T-Tauri star, a younger Class I protostar and a starless core within a very isolated filament and molecular cloud, and with an evolutionary gradient from southwest to northeast.

Figure 2 shows the dense starless core with green contours as observed by JCMT at 850 μm, which is embedded within a longer more diffuse filament seen by Herschel. This isolated filament, seen also in Figure 1 is oriented at ≈67° E of N. Planck polarization observations also show a large-scale magnetic field roughly parallel to the filament, although curving slightly to the south. The magnetic field of the starless core was previously observed using the predecessor to POL-2, SCUPOL, by Ward-Thompson et al. (2000) and a magnetic field strength in the core was calculated to be ≈160 μG (Crutcher et al. 2004). Additionally, Ward-Thompson et al. (2000) suggested that the magnetic field might be affected by the outflow of the RNO 91 source, although the entire molecular cloud was not observed and RNO 91 was on the very edge of the SCUPOL observations. The southern, blueshifted lobe of the CO outflow from RNO 91 (Lee et al. 2002) is seen in Figure 2 where RNO91 and 90 are also both labeled.

3. Observations and Data Reductions

3.1. SCUBA-2/POL-2 Observations

We observed L43 at 450 and 850 μm using the Submillimetre Common-User Bolometer Array 2 (SCUBA-2)/POL-2 on JCMT; however, this work focuses only on the 850 μm observations, and we leave the 450 μm data for a potential future multiwavelength study. The observations were taken between 2020 February and 2021 March as part of the BISTRO large survey program (Project ID: M20AL018) in its third generation of observations, "BISTRO-3." The observations consisted of 27 repeats of ∼31 minutes with one observation listed as questionable which we omitted from the data reduction. The data were observed in Band 1 weather conditions with the atmospheric opacity at 225 GHz (τ_{225}) less than 0.05. The JCMT has a primary dish diameter of 15 m and a beam size of 14.″6 at 850 μm when approximated with a two-component Gaussian (Dempsey et al. 2013). The observations were performed using a modified SCUBA-2 DAISY mode (Holland et al. 2013) optimized for POL-2 (Friberg et al. 2016), which produces a central 3′ region with uniform coverage with noise and exposure time increasing and decreasing, respectively, to the edge of the map. The 3′ region covers most of the L43 molecular cloud including the starless core and RNO 91. This mode has a scan speed of 8″ s^{-1} with a half-wave plate rotation frequency of 2 Hz (Friberg et al. 2016).

3.2. Data Reduction

To reduce the data, we used the Submillimetre User Reduction Facility (SMURF) package (Chapin et al. 2013) from the Starlink software (Currie et al. 2014). The SMURF package contains the data reduction routine for SCUBA-2/POL-2 observations named *pol2map*.[101]

In the first step, the raw bolometer time streams are separated into Stokes I, Q, and U time streams. The command *makemap* (Chapin et al. 2013) is then called to create an initial Stokes I map from the Stokes I time streams. The Stokes I map from the first step is used to create an AST and PCA mask at a fixed signal-to-noise ratio (S/N), which is then used to mask out nonastronomical signals (we refer to these as the auto-generated masks). The AST mask is used to define background regions that are forced to zero after each iteration in order to prevent growth of spurious structures in the map. The PCA mask is used to define regions that are excluded from the principle component analysis (PCA), which removes correlated large-scale noise components from the bolometer time streams. These excluded regions are generally source regions since these contain uncorrelated data and would disrupt the PCA process. The second step of the reduction creates the final Stokes I, Q, and U maps and a polarization half-vector catalog. The polarization vectors are often referred to as "half-vectors" due to the 180° ambiguity since direction is not known (e.g., 45° is treated the same as 225°). We included the parameter *skyloop* and followed the same data reduction technique as Pattle et al. (2021). We also set the parameter *pixsize* to a value of 8 to reduce the data with 8″ pixels as explained in Section 3.3.

We corrected for instrumental polarization (IP) in the Stokes Q and U maps based on the final Stokes I map and the "August 2019" IP polarization model.[102] The 850 μm Stokes I, Q, and U maps were also multiplied by a flux conversion factor (FCF) of 748 Jy beam^{-1} pW^{-1} to convert from pW to Jy beam^{-1} and account for loss of flux from POL-2 inserted into the telescope. This value was calculated using the post-2018 June 30 SCUBA-2 FCF of 495 Jy beam^{-1} pW^{-1} (Mairs et al. 2021) multiplied by a factor of 1.35 to account for the additional losses in POL-2 (Friberg et al. 2016) and then multiplied by a factor of 1.12 to account for the 8″ pixels. This extra factor was determined from SCUBA-2 calibration plots.[103] The final Stokes I map has an rms noise of ≈2.2 mJy beam^{-1}. To further increase the S/N of our polarization half-vectors and attempt to account for the JCMT beam size, we binned them to a resolution of 12″. The polarization half-vectors are also debiased as described in Wardle & Kronberg (1974) to remove statistical bias in regions of low S/N (see Equation (1)).

The values for the debiased polarization fraction P were calculated from

$$P = \frac{1}{I}\sqrt{Q^2 + U^2 - \frac{Q^2\delta Q^2 + U^2\delta U^2}{Q^2 + U^2}}, \tag{1}$$

where I, Q, and U are the Stokes parameters, and δQ, and δU are the uncertainties for Stokes Q and U. The uncertainty δP of the polarization degree was obtained using

$$\delta P = \sqrt{\frac{(Q^2\delta Q^2 + U^2\delta U^2)}{I^2(Q^2 + U^2)} + \frac{\delta I^2(Q^2 + U^2)}{I^4}}, \tag{2}$$

with δI being the uncertainty for the Stokes I total intensity.

The polarization position angles θ, measured from north to east in the sky projection (north is 0°), were measured using the relation

$$\theta = \frac{1}{2}\tan^{-1}\frac{U}{Q}. \tag{3}$$

The corresponding uncertainties in θ were calculated using

$$\delta\theta = \frac{1}{2}\frac{\sqrt{Q^2\delta U^2 + U^2\delta Q^2}}{(Q^2 + U^2)} \times \frac{180^\circ}{\pi}. \tag{4}$$

The plane-of-sky orientation of the magnetic field is inferred by rotating the polarization angles by 90° (assuming that the polarization is caused by elongated dust grains aligned perpendicular to the magnetic field).

3.3. Use of 8″ Pixels

Standard reductions of SCUBA-2/POL-2 observations are done with a 4″ pixel size (e.g., Pattle et al. 2021). Nearly all of these reductions have been done on bright, high S/N sources. As we approach the limit of the POL-2 polarimeter, we can explore the use of larger pixel sizes to attempt to boost the S/N in these dense, starless sources. The use of different pixel sizes in reductions of JCMT SCUBA-2 data has been explored before, such as in the Gould Belt Survey (Ward-Thompson et al. 2007) where originally 6″ (see Sadavoy et al. 2013) and 3″ (see Mairs et al. 2015) pixels were used with the latter being chosen in order to recover small-scale structure. The current pixel size of 4″ was picked in order to properly sample the Gaussian beam and allow the mapmaking algorithm to converge in a reasonable time (Chapin et al. 2013), as well as avoid smoothing of larger pixels. However, with faint sources such as starless cores, we need to investigate the potential of using larger pixel sizes.

One issue with using larger pixels is that the larger pixel size tends to produce masks that cover a larger area of the sky. Doubling the pixel size from 4″ to 8″ typically causes the number of bolometer samples falling in each pixel to increase by a factor of 4, thus increasing the S/N of each pixel value by a factor near to 2. Since each mask is defined by a fixed S/N cutoff, this causes a larger fraction of the map to be covered by the mask. An increase in the size of the AST mask is potentially problematic, as it can encourage the growth of artificial large-scale structures within the masked areas (see Chapin et al. 2013). Distinguishing such artificial structures from real astronomical signals requires care.

Our solution to this problem is to re-use the 4″ pixel auto-generated masks when creating externally masked maps with 8″ pixels, rather than using new masks based on the auto-masked 8″ maps. The smaller 4″ masks will then restrict the growth of artificial extended structures giving us more confidence in the remaining extended structure. To do this, we ran the entire reduction using the standard 4″ pixel size. We then regridded the AST and PCA masks from that reduction to 8″ using the command *compave* from the KAPPA package (Currie & Berry 2014). We then ran the second step of the reduction using the regridded AST and PCA masks to create the

[101] http://starlink.eao.hawaii.edu/docs/sun258.htx/sun258ss73.html http://starlink.eao.hawaii.edu/docs/sc22.htx/sc22.html

[102] https://www.eaobservatory.org/jcmt/2019/08/new-ip-models-for-pol2-data/

[103] https://www.eaobservatory.org/jcmt/instrumentation/continuum/scuba-2/calibration/

externally masked Stokes I, Q, and U maps as well as the polarization vector catalogs, using a pixel size of 8″. This resulted in a molecular cloud that looked similar to the original 4″ reduction but with better S/N and therefore more polarization half-vectors (vector catalog increased from 98 vectors to 133 vectors at the same S/N cut). This is the reduction that we present in this work.

As a further check, we performed a jackknife test by dividing our observations into two populations and comparing the Stokes I, Q, and U maps from both populations. The results from this test can be found in the Appendix. We saw a more significant difference between the populations when using the auto-masked 8″ maps. This difference occurred mainly in the areas where emission was present in the 8″ maps but not present in the 4″ maps, raising further doubt as to the validity of the new extended emission in the auto-masked 8″ maps. Any differences seen in 8″ reduction done using the regridded masks were the same as differences seen in 4″ reduction, just smoothed due to larger pixel sizes.

3.4. CO Observations

We used archival observations of the CO $J = 1$–0 line carried out with the Berkely Illinois Maryland Array (BIMA) 10 antenna interferometry array. The CO $J = 1$–0 data were obtained from Lee et al. (2002), and details of the observations and data reduction can be found therein. BIMA has a similar beam size to that of JCMT at 12.″8.

We also used archival observations of the CO $J = 3$–2 line carried out with the Heterodyne Array Receiver Program (HARP) to remove CO contribution from the 850 μm Stokes I map. This is discussed further in Section 4.3. The data were accessed from the Canadian Astronomy Data Centre database[104] (Project ID: M07AU11) and were downloaded as reduced spectral cubes that were then mosaicked using the PICARD recipe MOSAIC_JCMT_IMAGES.[105]

4. Results

4.1. 850 μm Dust Morphology

Figure 2 shows the 850 μm dust contours in green overlaid on the Herschel SPIRE 250 μm where the 850 μm dust traces the densest part of the filament. The filament does continue to the east and west, but this may be more extended structure and is therefore lost by SCUBA-2/POL-2. The 850 μm dust traces the northern edge of the CO outflow cavity, which is discussed in the next section. The 850 μm emission is peaked in the main starless core (L43) and then the dust region surrounding RNO 91.

Figure 3 shows the column density map, which is discussed later in Section 4.3 but it has the 850 μm dust contours overlaid with more levels to better show the emission structure. In the main starless core, the densest emission peaks toward the center, but then there are two lobes that extend to the northwest and southeast. A small peak can be seen in southeast lobe in Figure 3. We do not have resolved kinematic or significant magnetic field data between these three areas (the center part and the two lobes) so it is not possible to tell if they are fragmenting. However, the 850 μm emission shows structure suggesting these could be on the way to fragmentation.

[104] https://www.cadc-ccda.hia-iha.nrc-cnrc.gc.ca/en/jcmt/
[105] http://www.starlink.ac.uk/docs/sun265.htx/sun265ss15.html

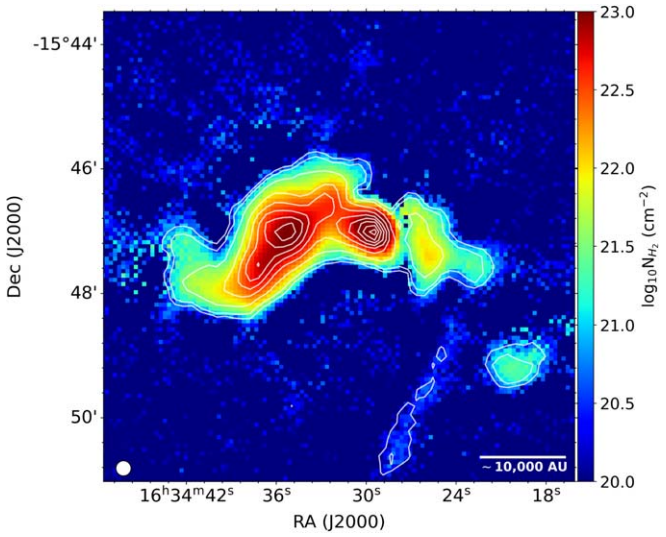

Figure 3. Molecular hydrogen column density map calculated from filtered Herschel Photodetector Array and Camera Spectrometer (PACS) 160 μm, SPIRE 250, 350, and 500 μm and SCUBA-2/POL-2 850 μm maps, with 850 μm contours overlaid. The method for calculating the H_2 column density is described in Section 4.3.

We can model these three regions as Bonnor–Ebert (BE) spheres (Ebert 1955; Bonnor 1956) and estimate their critical BE masses. We take the sound speed c_s to be $\sim$0.19 km s^{-1}, which was calculated assuming a dust temperature of 12.1 K (Planck Collaboration et al. 2016c). The critical BE mass can be calculated using the relation (Equation (3.9), Bonnor 1956),

$$M_{\rm BE,crit} = 3.3\frac{c_s^2}{G}R_{\rm crit}, \quad (5)$$

where G is the gravitational constant and $R_{\rm crit}$ is the critical radius of the core. We estimate $R_{\rm crit}$ from the observed flux structure (where the flux drops before peaking again in the center) and use it to also calculate total flux for total mass estimates. Values for $R_{\rm crit}$ are given in Table 1 along with locations of the three potentially fragmenting regions in the submillimeter core (northwest, main, and southeast). The estimated critical BE masses of the two lobes are $M^{\rm NW}_{\rm BE,crit} \sim 0.21\,M_\odot$ and $M^{\rm SE}_{\rm BE,crit} \sim 0.20\,M_\odot$ for the northwest and southeast lobes, respectively. For the central (main) peak, the estimated critical BE mass is $M^{\rm main}_{\rm BE,crit} \sim 0.32\,M_\odot$.

We can estimate the total mass from the 850 μm dust emission using the relation from Hildebrand (1983),

$$M_{\rm TOT} = \frac{F_\nu D^2}{\kappa_\nu B_\nu(T_{\rm d})}, \quad (6)$$

and see also Ward-Thompson & Whitworth (2011), where

$$\kappa_\nu = \kappa_o\left(\frac{\nu}{\nu_o}\right)^\beta, \quad (7)$$

and F_ν is the total measured flux density at the observed frequency ν, $B_\nu(T_{\rm d})$ is the Planck function for a dust temperature $T_{\rm d}$ ($T_{\rm d}$ = 12.1 K Planck Collaboration et al. 2016c), and κ_ν is the monochromatic opacity per unit mass of dust and gas. $\kappa_\nu \sim 0.0125$ cm^2 g^{-1} assuming $\kappa_o = 0.1$ cm^2 g^{-1}, $\nu_o = 10^{12}$ Hz (Beckwith et al. 1990) and $\beta = 2$. We should note

Table 1
Mass Estimates

	SMM Core Sources			Protostellar Sources	
	NW Lobe[a]	Main[a]	SE Lobe[a]	RNO 90	RNO 91[a]
R.A. (J2000)	16:34:32.73	16:34:35.33	16:34:37.16	16:34:09.29	16:34:29.57
Decl. (J2000)	−15:46:31.0	−15:46:58.72	−15:47:32.2	−15:48:14.9	−15:46:58.6
$R_{\rm crit}$ ($''$)	12.8	19.6	12.0	…	…
R ($''$)	12.8	19.6	12.0	14.4	32.0 × 18.0 (60°)
$M_{\rm BE,crit}$[b] ($M_\odot$)	0.21	0.32	0.20	…	…
$M_{\rm TOT}$[c] ($M_\odot$)	0.10	0.37	0.12	0.033(0.016)	0.335(0.169)

Notes. $R_{\rm crit}$ is the critical radius of the object as described in Section 4.1 used to estimate critical BE masses. R is the observed radius of the source as based on the flux distribution. For RNO 91 we have listed the semimajor and semiminor axes of the ellipse with the position angle (east of north) in parentheses.
[a] Distance to source taken to be 125 pc (see Section 2).
[b] See Equation (5).
[c] See Equation (6).

that κ_ν can have a systematic uncertainty of up to 50% (Roy et al. 2014).

Assuming a distance of 125 pc, we estimate total masses from the 850 μm dust emission of $M_{\rm TOT}^{\rm NW} \sim 0.10\,M_\odot$ and $M_{\rm TOT}^{\rm SE} \sim 0.12\,M_\odot$ for the northwest and southeast lobes, respectively, and $M_{\rm TOT}^{\rm main} \sim 0.37\,M_\odot$ for the main core. This suggests that if they are indeed fragmented, the central part of the starless core may be undergoing gravitational collapse (i.e., $M_{\rm TOT}^{\rm main}/M_{\rm BE,crit}^{\rm main} > 1$) while the two smaller lobes are not, rather than a coherent collapse of the whole core. All of the masses are summarized in Table 1.

We also estimated the envelope mass from the 850 μm dust emission of the two T-Tauri sources RNO 90 and RNO 91 using Equation (6). We find a total estimated envelope mass for RNO 90 of $M_{\rm TOT}^{\rm RNO\ 90} = 0.033 \pm 0.016\,M_\odot$ assuming a distance of 115.7 ± 1 pc and a radius of $14\farcs4$. This is orders of magnitude greater than the dust mass of the disk as seen by the Atacama Large Millimeter/submillimeter Array (ALMA), which is closer to $2 \times 10^{-5}\,M_\odot$ (Garufi et al. 2022), but we do not resolve this structure and are more likely seeing the remaining dusty envelope. For RNO 91, we estimate a total mass from the 850 μm dust emission of $M_{\rm TOT}^{\rm RNO\ 91} = \sim 0.335 \pm 0.169\,M_\odot$ assuming a distance of 125 pc and that the dusty envelope is an ellipse with dimensions $32\farcs0 \times 18\farcs0$ rotated 60° east of north. This estimated total mass value is in good agreement with Young et al. (2006) who found a mass of $0.3 \pm 0.1\,M_\odot$. Assuming just a uniform sphere of radius $15\farcs6$, we get an estimated total mass of $0.215 \pm 0.109\,M_\odot$.

4.2. Outflow of RNO 91

As mentioned in Section 2, there is a weak CO outflow driven by the embedded Class I protostar in RNO 91. The southern outflow traces the southern edge of the L43 starless core and forms a limb-brightened U shape (Lee et al. 2002), which is seen in all transitions. The southern outflow is heavily blueshifted, indicating the outflow is tilted toward us, potentially by up to 60° (Lee & Ho 2005). Weintraub et al. (1994) found that RNO 91 is not very deeply embedded in the L43 molecular cloud and rather sits nearer to us than the main submillimeter starless core.

However, a very clear dust cavity can be seen in Figure 2, which the outflow traces nearly perfectly. This dust cavity sits along the filament, and it appears that the filament has been disrupted by the outflow, as material is cleared to the south and potentially pushed north to form the kink in the filament, though there is not much redshifted CO emission to the north. This morphology of the dust in the filament suggests some sort of interaction with or influence by the outflow. This does contradict the above claim that the source is not deeply embedded. The 850 μm dust emission also shows this U-shaped bend to the south, suggesting even the densest part of the filament is affected by, or was initially affected by, the outflow. Bence et al. (1998) did suggest that the outflow has been weakened over time by a UV radiation field, so the current outflow we observe may not be the original morphology or strength.

One possibility then is that the source was previously embedded and cleared out the dust cavity we see including along the LOS so that it presently sits in the foreground of the dense filament. This was also suggested by Mathieu et al. (1988) who determined that RNO 91 was once associated with the dense molecular core, but has since blown through the dense gas with the outflow. They also suggested that the outflow energy is only coupled with a small fraction of the core mass. So the majority of the dense starless core L43 is undisturbed, though as discussed later, our observations of the magnetic field suggest that we are either only tracing affected foreground dust or that the outflow has influenced some of the dense material.

Regardless, the fact that the dust appears to be heavily influenced by the outflow suggests we must be careful in our analysis of the magnetic field, which is traced by the dust. A more in-depth discussion of the interaction of the outflow with the magnetic field and potential CO emission or polarization contribution is presented in Section 5.2.

4.3. Dust Column Density

We used archival Herschel Photodetector Array and Camera Spectrometer (PACS) 160 μm, SPIRE 250, 350, and 500 μm dust emission maps,[106] along with the JCMT 850 μm dust emission map from this work to create column density maps. We filtered the Herschel maps in order to remove the large-scale structure that SCUBA-2/POL-2 is not sensitive to. We followed the method from Sadavoy et al. (2013) and Pattle et al. (2015) of introducing the Herschel maps into the Stokes I time stream and repeating the reduction process from Section 3.2, using $4''$ pixels. We then subtracted the original 850 μm

[106] From http://archives.esac.esa.int/hsa/whsa/.

only SCUBA-2/POL-2 Stokes I emission from the map, which included the Herschel maps in the reduction and the resulting map was the filtered Herschel map.

We also attempted to "correct" the 850 μm Stokes I maps by removing potential contamination from the ^{12}CO ($J = 3$–2) line. The ^{12}CO ($J = 3$–2) line, which sits at 345.796 GHz, is within the SCUBA-2 850 μm bandpass filter, so it can contribute to total intensity continuum. We followed the method of Parsons et al. (2018) using the HARP data mentioned in Section 3.4. We used the regular 4″ Stokes I map because this correction method is best characterized for 4″ maps before and for the purposes of fitting the blackbody spectrum, we do not require the increase in S/N that is helpful for our polarization vectors. The contribution to total intensity from CO was ∼5%–10%, getting up to ∼20% directly around RNO 91. We should note that the reduction produced slight negative bowling to the north of the L43 emission, though not in a region of any emission.

We then fit the five maps with a modified blackbody (Hildebrand 1983)

$$F_\nu = \mu_{\rm H_2} m_{\rm H} N_{\rm H_2} B_\nu(T_{\rm d}) \kappa_\nu, \quad (8)$$

where again F_ν is the measured flux density at the observed frequency ν, $B_\nu(T_{\rm d})$ is the Planck function for a dust temperature $T_{\rm d}$, $\mu_{\rm H_2}$ is the mean molecular weight of the hydrogen gas in the cloud, $m_{\rm H}$ is the mass of an hydrogen atom, $N_{\rm H_2}$ is the column density, and κ_ν is the dust opacity (see Equation (7)). We use a value of 2.8 for $\mu_{\rm H_2}$, and κ_ν was calculated for each frequency observed using Equation (7), where β is the emissivity spectral index of the dust and is taken to be 1.8 (an approximate value in starless cores; Shirley et al. 2005; Schnee et al. 2010; Sadavoy et al. 2013), and we again assume $\kappa_o = 0.1$ cm^2 g^{-1} and $\nu_o = 10^{12}$ Hz (Beckwith et al. 1990). We used temperature values from previously derived dust temperature maps using just the nonfiltered SPIRE maps and 850 μm maps, where we had convolved the data to the 500 μm resolution of ∼35″ and then regridded to the 850 μm maps.

We see column densities in the main starless core on the order of $10^{22.8}$ cm^{-2}, which is $\sim 6 \times 10^{22}$ cm^{-2}, with a maximum column density of $\sim 3 \times 10^{23}$ cm^{-2}.

4.4. Polarization Properties of the Starless Core

In Figure 4 we plot polarization fraction versus intensity of the nondebiased polarization half-vectors in L43. We focus only on the central 3′ region of L43, as this is where the exposure and noise are roughly uniform. A very clear decrease in polarization fraction can be seen toward the regions of high intensity. Within starless cores, this depolarization occurs in the highest density regions, due to some combination of field tangling and the loss of grain alignment at high enough A_V's (≈20 mag) as predicted by RAT theory (Andersson et al. 2015). A common method to study the grain alignment efficiency in molecular clouds is to determine the relationship between polarization efficiency and visual extinction, where polarization fraction and total intensity can be substituted for those two quantities, respectively, at submillimeter wavelengths (see Pattle et al. 2019 and references therein).

The relationship between polarization and intensity should follow a power law, $p \propto A_V^{-\alpha}$, where an α of 1 indicates a loss of alignment and an α of 0 would indicate perfect alignment.

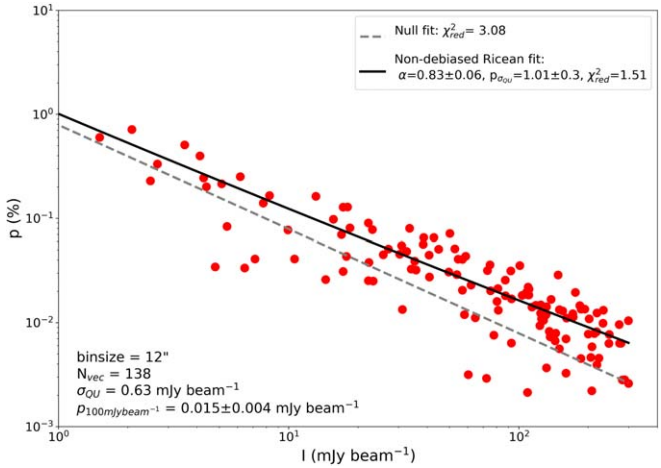

Figure 4. A plot of polarization fraction vs. Stokes I intensity of nondebiased polarization vectors in the inner 3′ area of the map. The vectors are binned to 12″, and the only selection criteria is Stokes $I > 0$. The null fit is plotted as a gray dashed line, while the Ricean fit is plotted as a black solid line. The α value for the Ricean and reduced-χ^2 values are given for both fits in the legend.

We follow the methods of Pattle et al. (2019) and use the Ricean fitting technique to fit the data. We get $\alpha = 0.83 \pm 0.06$ for the 12″ vectors and see an obvious offset from the null, which would indicate we retain some alignment. Additionally, the ordered polarization geometry suggests that we are continuing to trace the magnetic field to high A_V's. We performed the Ricean fitting for polarization vectors binned from 8″ up to 32″ and see α values from 0.89–0.70, respectively.

4.5. Magnetic Field Morphology

The vectors chosen for analysis have an S/N cut of $I/\delta_I > 10$ and $p/\delta_p > 2$. An S/N cut of $p/\delta_p > 2$ can be quite poor in polarization so we must proceed with caution with those vectors. In Figure 5 we plot the lower-S/N vector distribution (dashed histogram) and the higher-S/N vectors with $p/\delta_p > 3$ (solid histogram). Within most of the molecular cloud, the two S/N cuts agree well with the lower-S/N vectors following the same orientation as the higher-S/N vectors. The polarization angle distributions follow the same shape between the two S/N cuts, and they agree well with that found by Matthews et al. (2009) in the SCUPOL legacy survey (blue histogram). Using the lower-S/N cut, we get more data points to then use when calculating magnetic field strength (see Section 4.6), which could increase the spread of the position angles but can also increase the statistical confidence in the calculated dispersion.

As can be seen in Figure 5, there is no clear single morphology of the magnetic field, and it instead must be considered as either randomized or a multiple-component field. There is a rather distinct peak around 150° with then more scatter toward the lower magnetic field polarization angles. Some of this scatter is structured fields in other parts of the molecular cloud. As will be discussed later in Section 5.2, we suspect that the magnetic field is partially influenced by the CO outflow from RNO 91. This was discussed as well in Ward-Thompson et al. (2000), where they suggested the western edge of the field they observed was being influenced by RNO 91. With the more sensitive POL-2 observations and a larger field of view, we can actually see the overlap of the CO emission with some of the magnetic field vectors.

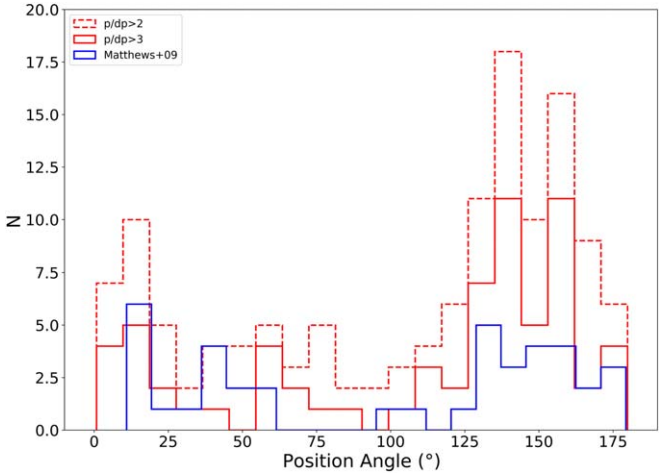

Figure 5. The distribution of the position angles of polarization half-vectors rotated by 90° to infer the magnetic field orientation. The dashed line distribution has an S/N cut of $I/\delta_I > 10$ and $p/\delta_p > 2$. The solid red line distribution has a stricter $p/\delta_p > 3$ S/N cut applied. The *B*-field position angle distribution from Matthews et al. (2009) are plotted in blue. The vector populations between the two S/N cuts appear consistent, suggesting that the lower-S/N vectors still trace the magnetic field. They also agree with the previous SCUPOL observations (Matthews et al. 2009).

We split the magnetic field inferred from the 850 μm polarized emission of L43 into three parts, the two labeled regions seen in Figure 6 and then the magnetic field vectors, which spatially (in the plane-of-sky) overlap with the CO outflow or are nearby and follow the same orientation. We list the mean field orientation, $\langle\theta_B\rangle$, and standard deviation from a Gaussian fit of the magnetic field position angle distributions in Table 2. Regions 1 and 2 show different magnetic field orientations, although both are rather scattered. Region 2, which corresponds to the northern half of the starless core, has a magnetic field that has an average orientation of 63° east of north, which is roughly parallel to the filament (≈67°) and Planck magnetic field orientations (≈60°). It also lies roughly perpendicular to the local core elongation axis, which is something seen across starless and prestellar cores (see Pattle et al. 2022a, for a recent review). This is further discussed in the context of the region's evolution in Section 5.3. There is more scatter toward the center of the region, which is what causes the spread we see in the position angles, but the structured component can be seen on either side.

Region 1 has a slightly more coherent magnetic field structure that is oriented ≈140° east of north, nearly perpendicular to the filament direction and parallel to the CO outflow. Considering it is still near to the CO outflow and is a less-dense region, the magnetic field could still be influenced by the CO outflow, or we are simply seeing another component of the complex magnetic field. The mean field orientation of the vectors spatially overlapping with the CO outflow is 146°, which is well aligned with the outflow direction, which we have taken to be $\sim 150° \pm 10°$ due to it curving slightly.

We also detect a few *B*-field vectors in the dust envelope of RNO 90 and in a very diffuse "blob," isolated to the west. RNO 90 is shown in the inset of Figure 6, and the magnetic field is oriented roughly north–south. The magnetic field in the diffuse blob to the west appears to still follow the large-scale Planck field, something that has been seen in diffuse cores (Ward-Thompson et al. 2023) and other isolated starless cores (L1689B; Pattle et al. 2021). The fact that this more diffuse region still follows the Planck field while Region 1 does not suggests that Region 1 may indeed be, or have been, affected by the outflow.

4.6. Magnetic Field Strength

We estimated the magnetic field strength in L43 using the Davis–Chandrasekhar–Fermi (DCF) method (Davis 1951; Chandrasekhar & Fermi 1953). The DCF method (see Equation (11)) assumes that the geometry of the mean magnetic field is uniform in each region. It then assumes that deviations from this uniformity are Alfvénic such that the deviations are due to nonthermal gas motions. The Alfvénic Mach number of the gas is given by

$$\mathcal{M}_A = \frac{\sigma_{NT}}{v_A} = \frac{\sigma_\theta}{Q}, \tag{9}$$

where the nonthermal deviations are quantified by a dispersion in magnetic field position angles, σ_θ. σ_{NT} is the 1D nonthermal velocity dispersion of the gas and Q is a correction factor that accounts for variations of the magnetic field on scales smaller than the beam and along the LOS where $0 < Q < 1$ (Ostriker et al. 2001). v_A is the Alfvén velocity of the magnetic field, and so $\mathcal{M}_A < 1$ suggests the magnetic field is more important than turbulent motions (sub-Alfvénic) while $\mathcal{M}_A > 1$ means the turbulent motions are more important (super-Alfvénic). The Alfvén velocity is given by

$$v_A = \frac{B}{\sqrt{4\pi\rho}} = Q\frac{\sigma_{NT}}{\sigma_\theta}, \tag{10}$$

where B is the magnetic field strength and ρ is the gas density. Since the dispersion in position angles, σ_θ, is for POS observations, we can only calculate the plane-of-sky magnetic field strength, B_{pos}, which is given by

$$B_{pos} \approx Q\sqrt{4\pi\rho}\,\frac{\sigma_{NT}}{\sigma_\theta}. \tag{11}$$

This can then be simplified to

$$B_{pos}(\mu G) \approx 18.6\, Q\sqrt{n(H_2)(cm^{-3})}\,\frac{\Delta v_{NT}(km\ s^{-1})}{\sigma_\theta(degree)}. \tag{12}$$

Typically Q is taken to be 0.5 (see Ostriker et al. 2001; Crutcher et al. 2004) but we will consider a range of Q values, $0.28 < Q < 0.62$ from Liu et al. (2022; see their Table 3) to obtain upper and lower limits of the *B*-field strength. Then $n(H_2)$ is the volume density of molecular hydrogen where $n(H_2) = \rho/\mu_{H_2} m_H$ and $\mu_{H_2} = 2.8$ and m_H is the mass of hydrogen. Δv_{NT} is the FWHM of the nonthermal gas velocity calculated by $\Delta v_{NT} = \sigma_{NT}\sqrt{8\ln 2}$. As mentioned above, σ_θ is the dispersion of the position angles of the magnetic field vectors, which we calculated using an angular dispersion function (ADF) as discussed later in this section. It should be noted that Crutcher et al. (2004) found on average $B_{pos}/B \approx \pi/4$, but since this is a general statistical correction, we do not use this when calculating the magnetic field strength.

We can rewrite Equations (9) and (10) as

$$\mathcal{M}_A = 1.74 \times 10^{-2}\sqrt{2}\ \frac{\sigma_\theta(degree)}{Q}, \tag{13}$$

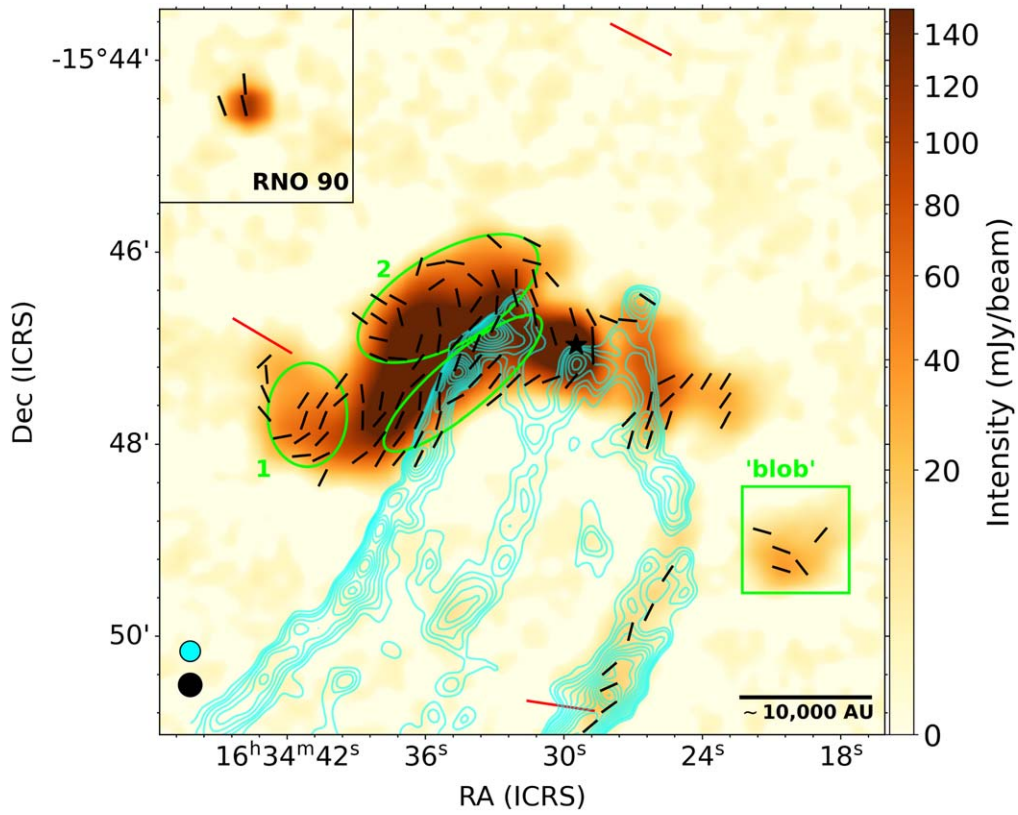

Figure 6. Magnetic field half-vectors are plotted in black with a uniform length over the 850 μm dust emission map. Planck vectors are the larger red vectors. The CO outflow continuum discussed in Section 4.2 is plotted with blue contours. Regions 1 and 2 are labeled, and the ellipses drawn are listed in Table 2. The third ellipse shows the area of the cloud we used to calculate column and volume densities for the outflow vectors. We also label the dust "blob" to the west, and RNO 90 is shown in the upper-left corner. The BIMA and JCMT beam sizes are shown in the lower left in blue and black, respectively.

Table 2
DCF+ADF Values

Region	Outflow	Reg 1	Reg 2
$\langle\theta_B\rangle$[a] (°)	146(22)	140(25)	63(24)
R.A. (J2000)	16:34:34.9	16:34:41.7	16:34:35.6
Decl. (J2000)	−15:47:30.0	−15:47:49.8	−15:46:37.1
a (″)	62.9	32.3	63.0
b (″)	17.4	24.8	28.8
PA[b] (°)	130	0	120
c (″)	33.1	25.7	42.6
$N(H_2)$ ($\times10^{21}$ cm^{-2})	33.0(7.0)	4.0(1.0)	52.0(9.0)
$n(H_2)$ ($\times10^5$ cm^{-3})	4.0(0.9)	0.57(0.15)	4.9(0.8)
Δv_{NT}[c] (km s^{-1})	0.35(0.02)	0.35(0.02)	0.35(0.02)
b (°)	14.0(1.5)	15.3(6.2)	23.8(4.0)
σ_θ (°)	10.1(1.1)	11.0(4.5)	17.6(3.0)
B_{pos} (μG)	116(20)–257(42)	40(17)–88(38)	73(14)–162(32)
$\mathcal{M}_A$	0.4(0.04)–0.9(0.1)	0.4(0.2)–1.0(0.4)	0.7(0.1)–1.6(0.3)
v_A (km s^{-1})	0.3(0.04)–0.7(0.1)	0.3(0.1)–0.7(0.3)	0.2(0.03)–0.4(0.1)
λ	⋯	0.3(0.2)–0.8(0.4)	2.4(0.6)–5.4(1.4)
E_B ($\times10^{35}$ J)	0.5(0.2)–2.6(0.9)	⋯	0.5(0.2)–2.2(0.9)

Notes.
[a] Standard deviation of the Gaussian fit is in parentheses.
[b] PA of ellipses is counterclockwise from north.
[c] Δv_{NT} values from Caselli et al. (2002).

and

$$v_A(\mathrm{km\ s^{-1}}) = 24.2Q\ \sqrt{2}\ \frac{\Delta v_{NT}(\mathrm{km\ s^{-1}})}{\sigma_\theta(\mathrm{degree})}, \quad (14)$$

respectively. We have also included a $\sqrt{2}$ factor in Equations (13) and (14), which is suggested by Heiles & Troland (2005) to account for the velocity line width assumptions, specifically converting the 1D LOS velocity measurements to an approximate value suitable for estimating the POS magnetic field strength.

We calculated the magnetic field strength in Regions 1 and 2 (shown in Figure 6) using Equation (12). We treated the regions as ellipses with semimajor and semiminor axes a and b (see Table 2), and assumed the depth of those regions to be the geometric mean, $c = \sqrt{ab}$. We used column density values from Figure 3 to calculate the volume density, $n(H_2)$, in each region. We used N_2H^+ (1–0) velocity line profiles from Caselli et al. (2002), which have a resolution of ~0.063 km s^{-1}. We corrected them to account for the thermal component (since Equation (12) uses nonthermal velocity line widths), which was calculated using the excitation temperature, $T_{ex} = 7 \pm 1$ K (also from Caselli et al. 2002), giving 0.35 ± 0.02 km s^{-1}. It should be noted that the velocity line profile observations are from the main starless core (Region 2). These observations do not necessarily extend to Region 1, but we do not have observations of Region 1 specifically so elect to use the same line width value as Region 2. Line widths of other tracers in the main starless core vary with some larger than and some smaller than the 0.35 km s^{-1} value we use (see Chen et al. 2009), but

N_2H^+ (1–0) traces dense regions of molecular clouds, which should coincide with the depths we are observing at 850 μm as well. There are also NH_3 observations of the starless core from Jijina et al. (1999) and Fehér et al. (2022), with a spread of line width values from 0.273 km s^{-1} (HFS fitting from Fehér et al. 2022) to 0.718 km s^{-1} (Gaussian fitting from Fehér et al. 2022) and then 0.32 km s^{-1} (Jijina et al. 1999). Considering the largest line width, the B-field strength could be up to two times larger.

We determined the dispersion of position angles in each region using the ADF (Hildebrand et al. 2009; see their Equations (1) and (3)). This assumes that there is a large-scale structured field and a smaller turbulent or random component. We assume that the length scales we are observing with JCMT/POL-2 (ℓ) are greater than the turbulent correlation length and much smaller than the large-scale field (such as Planck). While the former statement may be more difficult to accurately determine, the latter is true in our situation as we see a very structured large-scale B-field from Planck (see Figure 2) with no variations in the region we are looking at (admittedly a single Planck beam nearly covers the whole region). The contribution of both the turbulent and large-scale components to the angular dispersion of B-field vectors $\langle \Delta\Phi^2(\ell)\rangle^{1/2}$ is given by the terms b and $m\ell$, respectively, and the relation (Hildebrand et al. 2009),

$$\langle \Delta\Phi^2(\ell)\rangle_{\rm tot} \simeq b^2 + m^2\ell^2 + \delta_\theta^2(\ell), \tag{15}$$

where $\delta_\theta^2(\ell)$ is the additional contribution to the dispersion from measurement uncertainties (see Equation (4)). In each region, we calculated $\langle \Delta\Phi^2(\ell)\rangle_{\rm tot}$ and then fit Equation (15) to determine values for m and b. The plots are seen in Figure 7 where the best-fit parameters are shown as well. In all three regions, limiting the fitting to the first three bins (36″) provides the best fit (as determined by $\chi^2 < 1$), though for the outflow region, extending the fit to 48″ still provided $\chi^2 < 1$. For this region we then take the mean of the b values from both fits (14.2 for 36″ and 13.7 for 48″) to get $b \approx 14.0 \pm 1.5$. Generally we see the dispersion slowly increase with distance (Hildebrand et al. 2009; Hwang et al. 2023; see also the top panel of Figure 7), but in the bottom two panels of Figure 7 we see the dispersion growing and then at a large distance, suddenly drop again. In the case of Region 2 (bottom panel of Figure 7), the distance this happens at, ∼120″, is the distance between the two structured components mentioned in Section 4.5, further justifying a structured field approximately oriented at 56° and parallel with the Planck field and the filament direction. The dispersion in magnetic field position angles, σ_θ, can then be calculated by

$$\sigma_\theta = \frac{b}{\sqrt{2 - b^2}} \frac{180^\circ}{\pi}, \tag{16}$$

where b (in radians) is found from the ADF fit (see Hildebrand et al. 2009; see also Figure 7).

The magnetic field strength in Regions 1 and 2 is ∼40–90 μG and ∼70–160 μG, respectively. All of the values calculated when considering the magnetic field strength are listed in Table 2. In our situation, the difference in magnetic field strength between regions is due to variations in density and angular dispersion of the vectors since we use a constant velocity line width value across the region. For example, despite the larger σ_θ in Region 2, it is also denser, which is what increases the magnetic field strength and makes it comparable, if not greater than, the magnetic field in Region 1. We calculate an upper and lower bound for each of our magnetic field strengths based on the variation in Q of $0.28 < Q < 0.62$ (Liu et al. 2022). The value in Region 2 is

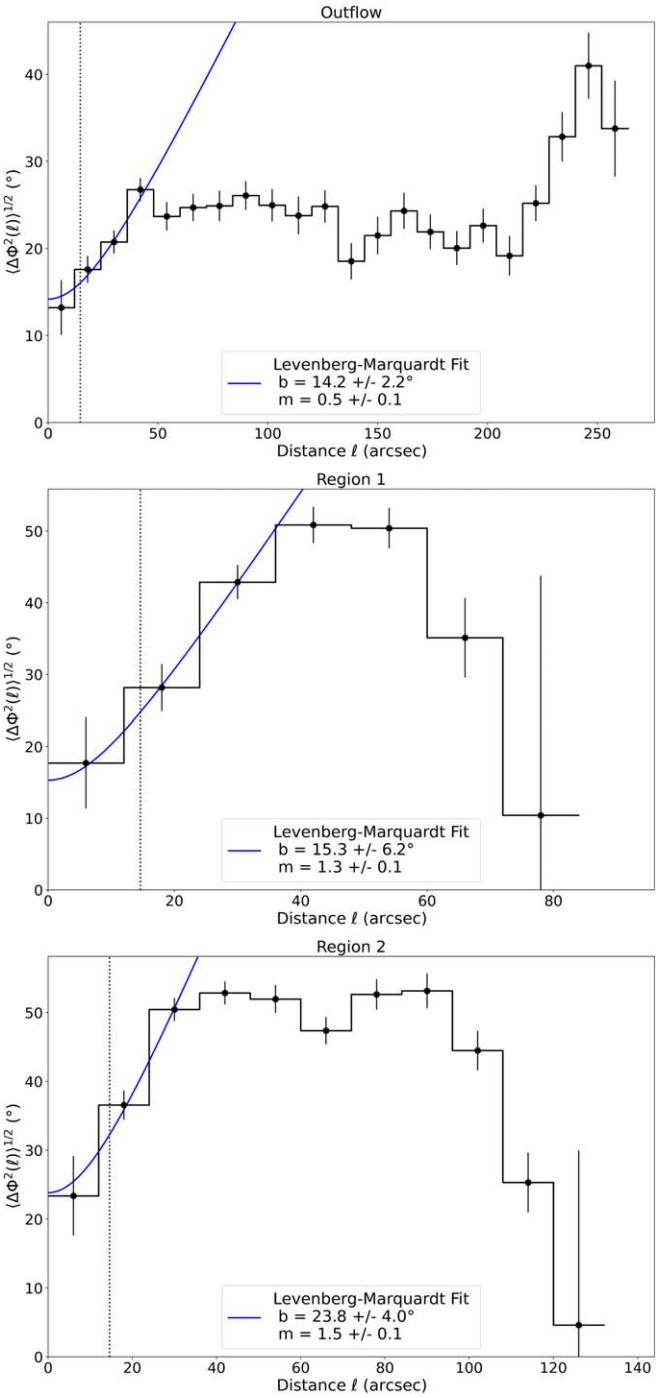

Figure 7. The angular dispersion function (ADF) histograms for various regions of interest in L43. All plots show fitting results when limiting the fit to the first three bins (36″). All fits were optimized with the Levenberg-Marquardt method and are weighted by the errors. Best-fit parameters are shown in the legend where b and m are from Equation (15). The JCMT beam size is plotted as a vertical dotted line in all three plots. Top: ADF results for the vectors spatially associated and aligned with the outflow. Middle: ADF results for vectors in Region 1 (see Figure 6). Bottom: ADF results for vectors in Region 2 (see Figure 6).

approximately that found by Crutcher et al. (2004), although they treated the region as a sphere and had a smaller dispersion angle of 12°. We find a slightly larger column and volume density, by a factor of ∼1.3.

The magnetic field strength calculated for the outflow is ∼120–260 μG. However, we note that this value may be severely overestimated and its use for interpretation limited. This is because we do not generally apply the DCF method to regions interacting with outflows since we assume the deviations in the magnetic field to be small nonthermal gas motions in the region, and an outflow is a much stronger disruptive force. In our case, we are arguing that some of the dense gas and dust has been affected by the outflow and hence that the outflow may have dragged the field (which is flux-frozen into the gas), aligning it with the outflow walls and giving us the low position angle dispersion. In that case, the low position angle dispersion may be due to a strong outflow rather than a strong field; although this would require more outflow modeling to determine if the outflow would preferentially align and order the field, or disorder the field. Additionally, we consider all of the vectors spatially aligned with the outflow, but take just the dust density in the southern half of the L43 starless core. If we were to assume a much lower volume density, one that is more likely associated with outflow material, then our field strength would be lower.

We acknowledge the limitations of using the DCF method, especially when determining the position angle dispersion and acknowledge in such a low-S/N environment that these uncertainties are increased. However, we do find magnetic field strengths that are on the order of strengths seen in other starless cores (Karoly et al. 2020; Pattle et al. 2021), including values that agree within error with those found in Crutcher et al. (2004).

5. Discussion

5.1. Contribution of the Magnetic Field

The mass-to-flux ratio λ is a parameter that can be used to quantify the importance of magnetic fields relative to gravity (Crutcher 2004). It compares the critical value for the mass, which can be supported by the magnetic flux Φ, $M_{B_{\rm crit}} = \Phi/2\pi\sqrt{G}$ (Nakano & Nakamura 1978) to the observed mass and flux values. If the column density N and magnetic field strength B can be measured, the observed value for the ratio between mass and flux is $(M/\Phi)_{\rm obs} = mNA/BA$ and then the mass-to-flux ratio λ is,

$$\lambda = \frac{(M/\Phi)_{\rm obs}}{(M/\Phi)_{\rm crit}} = 7.6 \times 10^{-21} \frac{N_{\rm H_2}({\rm cm}^{-2})}{B_{\rm pos}(\mu{\rm G})} \quad (17)$$

where $m = 2.8\, m_{\rm H}$, $N_{\rm H_2}$ is the molecular hydrogen column density and $B_{\rm pos}$ is the plane-of-sky magnetic field strength. When $\lambda < 1$, then the magnetic field is strong enough to support against gravity; this is referred as a "magnetically subcritical" regime. Alternatively, if $\lambda > 1$, then the magnetic field is insufficient by itself to oppose gravity, and the cloud is instead "magnetically supercritical."

Using Equation (17), we calculate the mass-to-flux ratio to be 0.3–0.8 in the low-density periphery of the core, Region 1. We calculate a mass-to-flux ratio of 2.4–5.4 in the denser part of the core, Region 2. According to Crutcher (2004) these ratios can be overestimated due to geometric biases, and they suggest it can be overestimated by a factor up to 3, although it is a statistical correction and its application to individual measurements is unclear. If we consider this statistical correction, the mass-to-flux ratios are ∼0.1–0.3 and ∼0.8–1.8 in Regions 1 and 2, respectively. These are then the lower limits for the mass-to-flux ratio in each region.

We also get Alfvén Mach numbers of 0.4–1.0 and 0.7–1.6 for Regions 1 and 2, respectively, suggesting that both regions are roughly transcritical, and magnetic field and turbulence may play equal parts in support. As noted previously, the velocity information we are using is for the main starless core, which is near Region 2, but farther from Region 1, which is the low-density area on the periphery of the main dense core; it does not resolve individual parts of the molecular cloud. We also find Alfvén velocities in the range of 0.2–0.7 km s^{-1} throughout the cloud.

For the lower-density Region 1, the region is entirely magnetically subcritical, indicating that the region may still be sufficiently supported against gravitational collapse by the magnetic field. It is also slightly sub-Alfvénic, meaning the magnetic field may play the dominant role. In the denser Region 2, we obtain a more definitively supercritical mass-to-flux ratio (note the large uncertainties with this value, as well as the results of the statistical correction), with a lower limit approaching trans- to subcritical. This gradient of a subcritical envelope (Region 1) transitioning into a trans- to supercritical core (Region 2) at sufficient densities is described in Crutcher (2004). It does suggest that the magnetic field is not sufficiently strong to support against gravitational collapse in the main starless core. However, it is worth mentioning that there are still many other processes in the molecular cloud such as turbulence and the influence of the CO outflow that could prevent gravitational collapse into a stellar object. While we do not yet see a protostar-forming, as mentioned in Section 4.1, we do see some possible fragmentation within the starless core where the densest part may be undergoing gravitational collapse.

Myers (2017) suggested from modeling that L43 has formed all of the stars it will form in its lifetime and does not contain sufficient amounts of dense gas for further star formation. However, we find higher column density values than they use for their modeling and do see potential fragmentation in the core. Chen et al. (2009) found that the main L43 starless core has observed DCO^+ and HCO^+ abundances that are higher and lower than modeled abundances, respectively, for an assumed amount of CO depletion. They suggest this indicates more CO depletion in the core and that the L43 starless core is spending a longer time at the higher-density pre-protostellar core phase. If this is the case, additional supports such as turbulence may be needed to continue support against gravitational collapse in Region 2 since it seems to be moving beyond the stage where magnetic fields are critical. But findings of Region 2 in near equilibrium (within errors) also validates the long-lived age of the core that Chen et al. (2009) found. The local magnetic field appears to still be significant in the more diffuse Region 1, but this region is beyond the area considered by Chen et al. (2009). Additionally, we must consider that the CO outflow has potentially altered the structure of the magnetic field in the cloud, even within the starless core, potentially weakening or strengthening the field.

5.2. Interaction of the Magnetic Field with Outflows

The spatial alignment (in the plane-of-sky) of the magnetic field in L43 with the outflow cavity walls can be seen in Figure 6, where the cyan outflow spatially overlaps with many of the magnetic field vectors. The magnetic field vectors that coincide with the CO outflow show a uniform distribution and strong peak at 146°. This coincides well with the outflow direction, which we have taken to be $\sim 150^\circ \pm 10^\circ$ due to it curving slightly.

Weintraub et al. (1994) suggested that RNO 91 sits in the foreground of the general L43 molecular cloud and so the possibility exists that there is in fact no physical association between the magnetic field and outflow. However, as was mentioned in Section 4.1 and as can be clearly seen in Figure 2, the outflow appears to have carved a cavity out of the molecular cloud, indicating it is to some degree embedded. This was also suggested by Mathieu et al. (1988).

Alternatively, we may be tracing magnetic fields in the outflow cavity walls. In this case, as mentioned in Section 4.3, some of the Stokes *I* emission we see, especially in the regions coincident with the outflow cavity walls, may be CO features (Drabek et al. 2012), especially the isolated emission to the south of the main cloud. We expect some contribution to the measured Stokes *I* emission from CO, but such contributions are typically less than 20% of the total emission observed (Drabek et al. 2012; Pattle et al. 2015; Coudé et al. 2016) and in our case, we see contributions of ∼5%–15%. However, considering we do have some CO contribution, we cannot rule out the possibility that some fraction of the polarized emission in this region arises from CO polarization, polarized through the Goldreich-Kylafis effect (Goldreich & Kylafis 1981, 1982). This would add a further ±90° ambiguity on the magnetic field orientation.

On the other hand, we can assume the polarization and emission are not purely CO based, as the emission features are also seen in all of the Herschel bands and persist after CO subtraction in 850 μm, indicating that there is a real dust feature present. A similar "hollow shell" morphology of dust emission in the presence of outflows is discussed in Moriarty-Schieven et al. (2006). Additionally, Bence et al. (1998) suggested that the mere presence of CO suggests some amount of dust shielding (from the UV field) in the outflow region. Thus, we still consider it probable that we are tracing dust polarization in the outflow cavity walls.

Additionally, the relationship between magnetic fields with outflows has been observed on numerous occasions in other sources, on both JCMT and ALMA scales (see Hull et al. 2017, 2020; Lyo et al. 2021; Pattle et al. 2022b). Hull et al. (2017, 2020) and Pattle et al. (2022b) also saw a similar alignment between the magnetic field and the cavity wall of the outflow to that which we see in L43/RNO 91. The benefit of our larger field of view here, when compared to ALMA, is that we can compare the magnetic field of the outflow to that in the surrounding regions and see that there is not just a preferential direction northwest to southeast, but rather that the magnetic field in the outflow region is actually different to that in the rest of the cloud. It should be noted that in regions observed by the JCMT, a preferred misalignment of 50° between magnetic fields and outflows has previously been identified in a larger statistical sample (Yen et al. 2021). The outflow observations in that study are largely on envelope- or small scales (i.e., tens of arcseconds) rather than large-scale outflows like we see here. So while there is a statistically preferred misalignment between magnetic fields as observed by JCMT and outflows, we do not see a clear indication of this occurring in L43 and we instead see good alignment between outflow and magnetic fields. This is perhaps because we have such distinct large-scale cavity outflow walls, which is what JCMT may be preferentially tracing. RNO 91 would also be interesting to follow up with ALMA polarization observations since there are smaller-scale outflows in the envelope as well (Lee & Ho 2005; Arce & Sargent 2006). This could be more directly compared to observations by Hull et al. (2017, 2020) and to the statistical sample in Yen et al. (2021).

In RNO 91, the CO outflow was found to have a lower limit of its energy at $\approx 10^{29}$ J (Bence et al. 1998). However, this assumes a Class II source lifetime when considering how long the CO has been exposed to UV radiation, though a Class I lifetime would still be longer than the un-shielded CO lifetime of a few hundred years (Bence et al. 1998). So the CO outflow likely had a larger energy once and may have been able to influence the magnetic field orientation. Other studies have found the CO outflow energy to be $\sim 5 \times 10^{35}$ J (Myers et al. 1988) and $\sim 1.4 \times 10^{35}$ J (Arce & Sargent 2006). These values are comparable to the magnetic energy values we see in L43, which is what we would expect. We can calculate the magnetic energy in Region 2 and the outflow region using

$$E_{\rm B}({\rm J}) = 10^{-20} \frac{B^2(\mu{\rm G}^2)\, V({\rm m}^3)}{2\mu_o({\rm N\ A}^{-2})} \tag{18}$$

where B is the magnetic field strength in microGauss (as measured in the plane-of-sky), V is the volume of the region in cubic meters, and μ_o is the permeability of free space, giving us the magnetic energy in Joules. Since we consider the outflow to have affected the dense gas and dust and dragged the magnetic field, we would expect the outflow energy to be at least equal to the magnetic energy. Assuming an ellipsoid shape when calculating the volume of both regions (see Table 2 for ellipse parameters), we find magnetic energies of ≈ 0.5–2.5×10^{35} J. This suggests that we can help further place a lower limit on the outflow energy of ≈ 0.5–2.5×10^{35} J, which is comparable to the values stated above, though we do remain cautious of the magnetic field strength derived in the outflow region as mentioned before.

5.3. Evolution of This Isolated Filament

One point of interest in this region is that there is a very clear evolutionary gradient from southwest to northeast. Initially there is the evolved T-Tauri star RNO 90, which is the oldest source and currently has no known large-scale outflows. It has also formed a protostellar disk (Pontoppidan et al. 2010). RNO 91, which is farther along the filament, is a protostellar source that drives the now familiar CO outflow. Then finally the starless core sits ≈10,000 au farther along the filament. The orientation of this filament is such that it extends roughly radially away from Sco OB2, with RNO 90 the closest to Sco OB2. The filament sits ≈42 pc away from Sco OB2 (in the plane-of-sky) assuming a general distance of 125 pc. While this may be merely a coincidence, it is interesting that the evolutionary track in such an isolated filament starts in the part of the filament pointing directly toward Sco OB2 (in the plane-of-sky). The Ophiuchus region and star formation within

has previously been suggested to be shaped and driven by Sco OB2 (Loren 1989).

Additionally, we can picture two evolutionary scenarios for the starless core, scenarios that with present observations we cannot distinguish between and that may very well be happening at the same time. The starless core L43 has formed with its long axis parallel to the outflow cavity wall. This could suggest that material has been funnelled down the filament that is also parallel with the large-scale Planck field and is building up on the outflow cavity walls. Build-up has not occurred so readily along the western wall of the outflow cavity because there is less material available for accretion to the west since RNO 90 has already been formed. However, it could also be the case that the dense core already existed and fragmented to form both the starless core and RNO 91 and the starless core has not been compressed along the filament orientation by the outflow. It is difficult to differentiate between these two scenarios and the possibility of course remains that they could both be true, with an initial fragmentation that has become denser over time. Kim et al. (2020) suggested that the starless core is a "late" or chemically evolved starless core as determined by a high $N(\mathrm{DNC})/N(\mathrm{HN^{13}C})$ ratio and line detection in N_2D^+. So the core may have formed at a similar time to RNO 91 but has since had its evolution slightly delayed due to injected turbulence by RNO 91 as well as less readily available material to form a star with.

6. Summary

We presented polarization measurements of the infrared dark molecular cloud L43 at 850 μm made using JCMT/POL-2 as part of the JCMT BISTRO Survey. We found H_2 column densities on the order of 10^{22}–10^{23} cm^{-2}, which are typical values in dense starless cores. We measured a power-law index of ~ -0.85 when plotting polarization percentage as a function of total 850 μm intensity, indicating a possible decrease, but not complete loss, in grain alignment efficiency, deep within the molecular cloud. By rotating the polarization vectors by 90°, we inferred the magnetic field orientation in L43 and saw a complicated and multiple-component magnetic field.

We divided the magnetic field into three regions, with one region slightly offset from the dense submillimeter-bright core (Region 2), another region in the more diffuse region to the east (Region 1), and then vectors that spatially coincide in the plane-of-sky with the CO outflow driven by RNO 91. We saw alignment between the magnetic field and the outflow cavity walls that is distinctly different from the magnetic field in the rest of the cloud. We calculated the magnetic field strengths of $\sim 40 \pm 20$–90 ± 40 μG in Region 1 and $\sim 70 \pm 15$–160 ± 30 μG in Region 2. We calculated a magnetic field strength in the outflow region of $\sim 120 \pm 20$–260 ± 40 μG, but advise caution with interpreting this value. Region 1 appeared to be magnetically sub- or transcritical but sub-Alfvénic. This suggests that the magnetic field is still important in comparison to gravity and turbulent motions. Region 2 is both magnetically supercritical and sub- to trans-Alfvénic, so the magnetic field may not be playing a significant role. This is compounded by potential fragmentation in the main core, suggesting it could be heading toward forming a protostar. We also proposed an evolutionary gradient across the isolated filament starting with the most evolved source RNO 90, which is closest to the Sco OB2 association and moving away from Sco OB2 toward RNO 91 and then eventually the starless core.

Acknowledgments

We thank the referee for providing thoughtful and constructive feedback that helped improve this article. J.K. acknowledges funding from the Moses Holden Studentship for his PhD. D.W.-T. acknowledge Science and Technology Facilities Council (STFC) support under grant No. ST\R000786\1. K.P. is a Royal Society University Research Fellow, supported by grant No. URF\R1\211322. C.W.L. acknowledges the support by the Basic Science Research Program through the National Research Foundation of Korea (NRF) funded by the Ministry of Education, Science and Technology (NRF-2019R1A2C1010851), and support by the Korea Astronomy and Space Science Institute grant funded by the Korea government (MSIT; project No. 2022-1-840-05). W.K. was supported by the National Research Foundation of Korea (NRF) grant funded by the Korea government (MSIT) (NRF-2021R1F1A1061794). K.Q. is supported by National Key R&D Program of China Nos. 2022YFA1603100 and 2017YFA0402604, the National Natural Science Foundation of China (NSFC) grant U1731237, and the science research grant from the China Manned Space Project with No. CMS-CSST-2021-B06. C.L.H.H. acknowledges the support of the NAOJ Fellowship and JSPS KAKENHI grants KG18K13586, KG20K14527, and KG22H01271. M.R. is supported by the international Gemini Observatory, a program of NSF's NOIRLab, which is managed by the Association of Universities for Research in Astronomy (AURA) under a cooperative agreement with the National Science Foundation, on behalf of the Gemini partnership of Argentina, Brazil, Canada, Chile, the Republic of Korea, and the United States of America. L.F. acknowledges support from the Ministry of Science and Technology of Taiwan, under grant Nos. 111-2811-M-005-007 and 109-2112-M-005-003 -MY3. M.T. is supported by JSPS KAKENHI grant Nos. 18H05442, 15H02063, and 22000005. J.K. is supported by JSPS KAKENHI grant No. 19K14775. D.J. is supported by NRC Canada and by an NSERC Discovery Grant. E.J.C. is supported by Basic Science Research Program through the National Research Foundation of Korea (NRF) funded by the Ministry of Education (grant No. NRF-2022R1I1A1A01053862). F.P. acknowledges support from the Spanish State Research Agency (AEI) under grant No. PID2019-105552RB-C43 and from the Agencia Canaria de Investigación, Innovación y Sociedad de la Información (ACIISI) under the European FEDER (FONDO EUROPEO DE DESARROLLO REGIONAL) de Canarias 2014-2020 grant No. PROID2021010078. C.E. acknowledges the financial support from grant RJF/2020/000071 as a part of Ramanujan Fellowship awarded by Science and Engineering Research Board (SERB), Department of Science and Technology (DST), Govt. of India. The James Clerk Maxwell Telescope is operated by the East Asian Observatory on behalf of The National Astronomical Observatory of Japan; Academia Sinica Institute of Astronomy and Astrophysics; the Korea Astronomy and Space Science Institute; the National Astronomical Research Institute of Thailand; Center for Astronomical Mega-Science (as well as the National Key R&D Program of China with No. 2017YFA0402700). Additional funding support is provided by the Science and Technology Facilities Council of the United Kingdom and participating universities and organizations in the United Kingdom, Canada, and Ireland. The authors wish to recognize and acknowledge the very significant cultural role and reverence that the summit of

Maunakea has always had within the indigenous Hawaiian community. We are most fortunate to have the opportunity to conduct observations from this mountain. The data taken in this paper were observed under the project code M20AL018. The Starlink software (Currie et al. 2014) is currently supported by the East Asian Observatory.

Facilities: JCMT (SCUBA-2, POL-2), Herschel (SPIRE, PACS).

Software: Starlink (Currie et al. 2014), Astropy (Astropy Collaboration et al. 2013, 2018).

Appendix
8″ Stokes *I* Maps

Our initial concern over using a reduction that made use of auto-generated masks from an initial 8″ Stokes *I* map was that the emission was much more extended than in the 4″ maps. We do not expect to recover much large-scale flux due to inherent limitations with SCUBA-2/POL-2 and observing through the atmosphere. SCUBA-2 is fundamentally unable to measure flux on size scales larger than the array size due to the need to distinguish between atmospheric and astrophysical signals (Chapin et al. 2013; Holland et al. 2013), and POL-2 is even more restricted due to its small map size and slow mapping speed (Friberg et al. 2016). There are detailed discussions of SCUBA-2 large-scale flux loss compared to Herschel in Sadavoy et al. (2013) and Pattle et al. (2015), and detailed discussion of the role of masking in SCUBA-2 data reduction in Mairs et al. (2015) and Kirk et al. (2018). The first two images in the bottom panel of Figure A1 demonstrate the additional large-scale flux we see when using auto-generated 8″ masks, where the contours from the Stokes *I* continuum created using the regridded 4″ masks are plotted over the Stokes *I* continuum resulting from reducing the data using the auto-generated 8″ masks. The contour levels are the same as those shown in Figure 3. The background map for both the even and odd groups clearly shows emission beyond the extent of the drawn contours.

However, it can also be seen that this extended emission that we see from the contours aligns well with the SPIRE 250 μm image as mentioned in Section 3.3. It can be seen from Figure 2 that the 250 μm dust emission extends farther to the east from where the 850 μm contours end and follows the same shape that we see from the 8″ emission in Figure A1. We also see this dust morphology in all of the Herschel bands. However, it does not follow that the POL-2 Stokes *I* data in these regions is well characterized, because Herschel is able to observe extended structure.

As mentioned in Section 3.3, to further investigate this, we performed a jackknife test on the data. We divided the 26 observations into two groups, which we have designated as "even" and "odd." We divided the observations by just alternating between "even" and "odd" when the observations were ordered by date of observation. In each group, we then reduced the observations using the normal method described in Section 3.2 with both 4″ pixels and with 8″ pixels. Then for each group we reduced the observations using the new method (see Section 3.3), where we regridded the masks from the 4″ reduction in each group to 8″ and used those masks when running an 8″ reduction instead of using the auto-generated 8″ masks.

Figure A2 shows the results of the jackknife test in Stokes *I* maps for the reduction method presented in this work. Figure

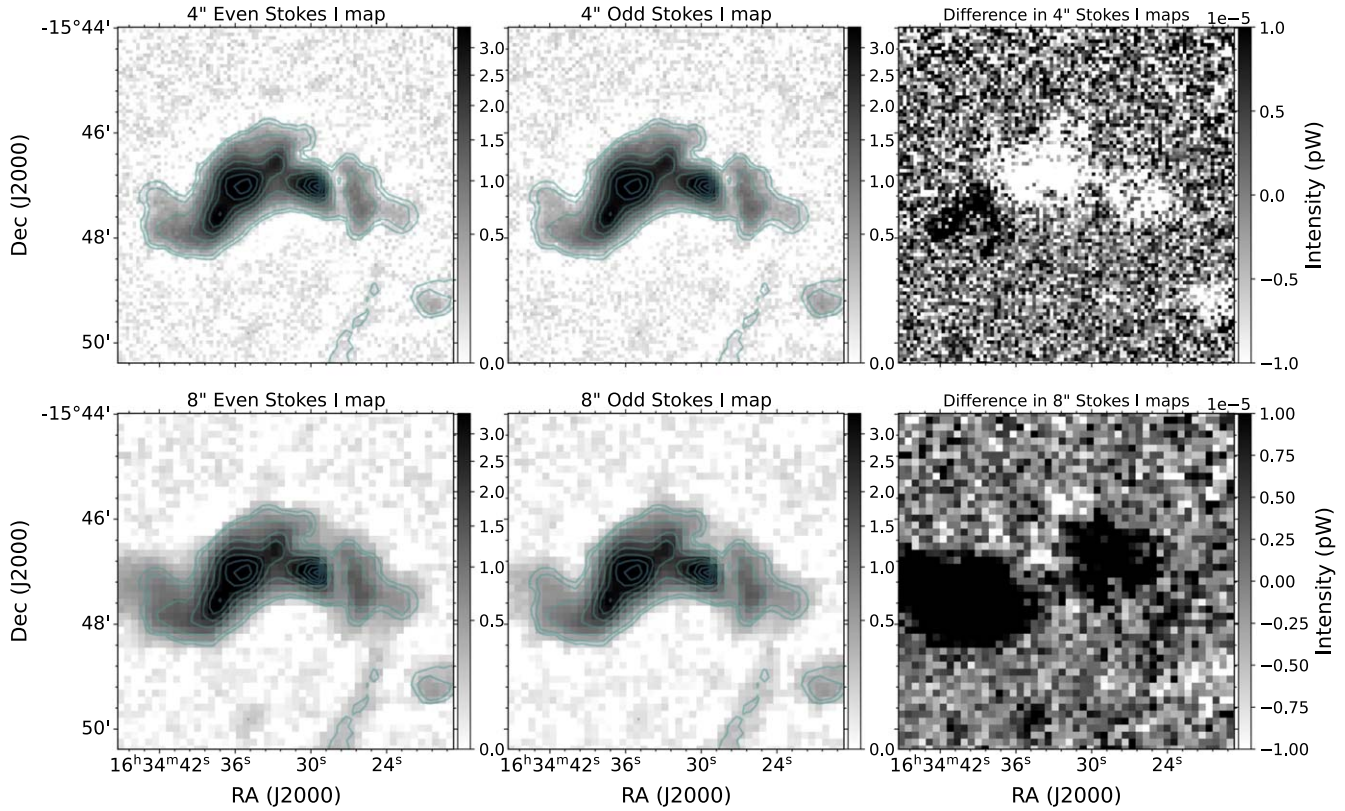

Figure A1. Results of the jackknife test for the data reduction technique using the auto-generated 8″ masks when reducing with 8″ pixels. The top row of panels shows the 4″ Stokes *I* maps from the even and odd groups as well as the difference between the groups. The color scales on the even and odd maps are $\times 10^{-4}$ pW.

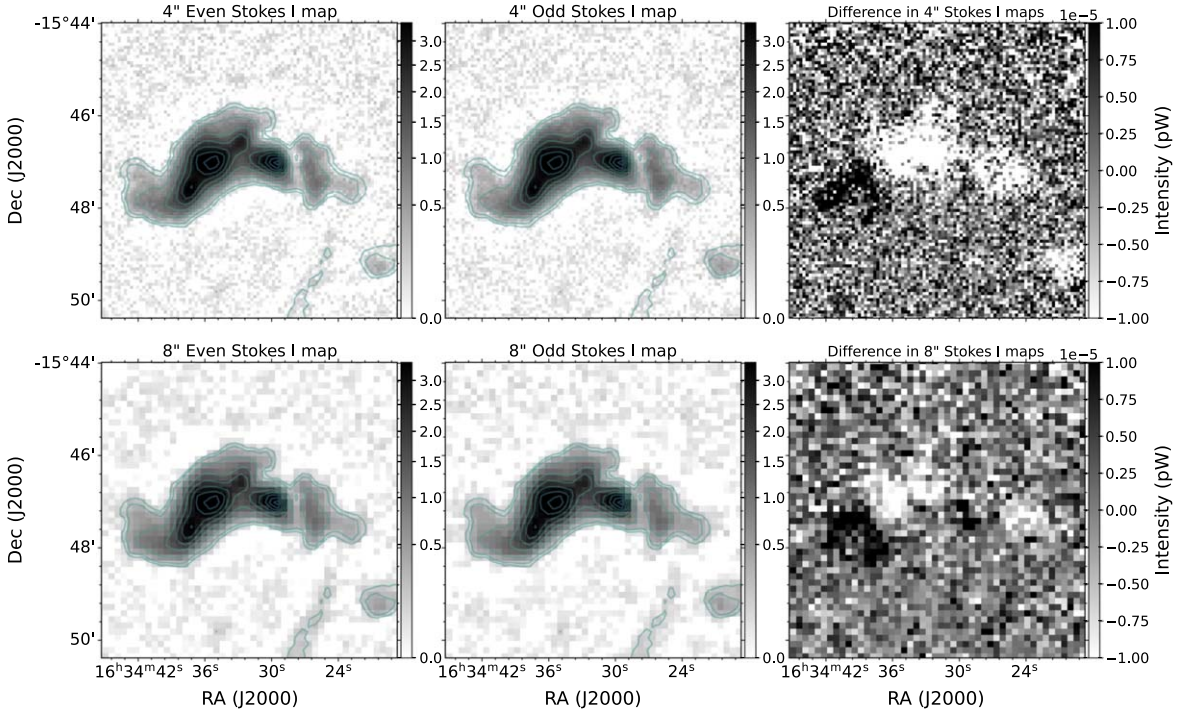

Figure A2. Results of the jackknife test for the data reduction technique presented in Section 3.3. The top row of panels shows the 4″ Stokes *I* maps from the even and odd groups as well as the difference between the groups. The bottom row of panels shows the 8″ Stokes *I* maps and the difference between them. The color scales are the same as Figure A1.

A1 then shows the results of the jackknife test, but using the 8″ pixel auto-generated masks. The upper rows in Figures A1 and A2 are the same and show the Stokes *I* map from a standard 4″ reduction. All of the images have the same color map scale, and the difference map is the odd map subtracted from the even map. Stokes *Q* and *U* emission is very weak in starless cores, and so little difference was seen between the two methods.

In Figure A2, there is some difference seen between the "even" and "odd" maps with the normal 4″ reduction, but this same difference can be seen in the regridded 8″ reduction, just slightly blurred due to the larger pixel sizes. The difference is most likely due to the group selection and would change with different grouping. However, in Figure A1, the difference in the auto-generated 8″ mask reduction is very different from the 4″ reduction. Additionally, the difference is seen in the areas of extended emission that appear in the normal 8″ reductions but not in the 4″ reduction (as traced by the contours). This difference is why we raise concerns with blindly increasing the value of the *pixsize* parameter in the data reduction and potentially producing artificial structures. A different jackknife test grouping may yield a different residual map, or one that is not so severe. Future reduction tests can be conducted to determine if it is a selection effect or in fact growth of a nonastronomical signal.

ORCID iDs

Janik Karoly https://orcid.org/0000-0001-5996-3600
Derek Ward-Thompson https://orcid.org/0000-0003-1140-2761
Kate Pattle https://orcid.org/0000-0002-8557-3582
David Berry https://orcid.org/0000-0001-6524-2447
Anthony Whitworth https://orcid.org/0000-0002-1178-5486
Jason Kirk https://orcid.org/0000-0002-4552-7477
Pierre Bastien https://orcid.org/0000-0002-0794-3859
Tao-Chung Ching https://orcid.org/0000-0001-8516-2532
Simon Coudé https://orcid.org/0000-0002-0859-0805
Jihye Hwang https://orcid.org/0000-0001-7866-2686
Woojin Kwon https://orcid.org/0000-0003-4022-4132
Archana Soam https://orcid.org/0000-0002-6386-2906
Jia-Wei Wang https://orcid.org/0000-0002-6668-974X
Tetsuo Hasegawa https://orcid.org/0000-0003-1853-0184
Shih-Ping Lai https://orcid.org/0000-0001-5522-486X
Keping Qiu https://orcid.org/0000-0002-5093-5088
Doris Arzoumanian https://orcid.org/0000-0002-1959-7201
Tyler L. Bourke https://orcid.org/0000-0001-7491-0048
Huei-Ru Vivien Chen https://orcid.org/0000-0002-9774-1846
Wen Ping Chen https://orcid.org/0000-0003-0262-272X
Jungyeon Cho https://orcid.org/0000-0003-1725-4376
Eun Jung Chung https://orcid.org/0000-0003-0014-1527
Victor Debattista https://orcid.org/0000-0001-7902-0116
James Di Francesco https://orcid.org/0000-0002-9289-2450
Pham Ngoc Diep https://orcid.org/0000-0002-2808-0888
Yasuo Doi https://orcid.org/0000-0001-8746-6548
Chakali Eswaraiah https://orcid.org/0000-0003-4761-6139
Lapo Fanciullo https://orcid.org/0000-0001-9930-9240
Laura M. Fissel https://orcid.org/0000-0002-4666-609X
Tim Gledhill https://orcid.org/0000-0002-2859-4600
Thiem Hoang https://orcid.org/0000-0003-2017-0982
Martin Houde https://orcid.org/0000-0003-4420-8674
Charles L. H. Hull https://orcid.org/0000-0002-8975-7573
Tsuyoshi Inoue https://orcid.org/0000-0002-7935-8771
Shu-ichiro Inutsuka https://orcid.org/0000-0003-4366-6518
Kazunari Iwasaki https://orcid.org/0000-0002-2707-7548
Il-Gyo Jeong https://orcid.org/0000-0002-5492-6832
Doug Johnstone https://orcid.org/0000-0002-6773-459X
Ji-hyun Kang https://orcid.org/0000-0001-7379-6263

Miju Kang https://orcid.org/0000-0002-5016-050X
Akimasa Kataoka https://orcid.org/0000-0003-4562-4119
Francisca Kemper https://orcid.org/0000-0003-2743-8240
Jongsoo Kim https://orcid.org/0000-0002-1229-0426
Shinyoung Kim https://orcid.org/0000-0001-9333-5608
Gwanjeong Kim https://orcid.org/0000-0003-2011-8172
Kyoung Hee Kim https://orcid.org/0000-0001-9597-7196
Kee-Tae Kim https://orcid.org/0000-0003-2412-7092
Florian Kirchschlager https://orcid.org/0000-0002-3036-0184
Masato I. N. Kobayashi https://orcid.org/0000-0003-3990-1204
Patrick M. Koch https://orcid.org/0000-0003-2777-5861
Jungmi Kwon https://orcid.org/0000-0003-2815-7774
Chang Won Lee https://orcid.org/0000-0002-3179-6334
Chin-Fei Lee https://orcid.org/0000-0002-3024-5864
Jeong-Eun Lee https://orcid.org/0000-0003-3119-2087
Sheng-Jun Lin https://orcid.org/0000-0002-6868-4483
Hong-Li Liu https://orcid.org/0000-0003-3343-9645
Tie Liu https://orcid.org/0000-0002-5286-2564
Sheng-Yuan Liu https://orcid.org/0000-0003-4603-7119
Junhao Liu https://orcid.org/0000-0002-4774-2998
Steven Longmore https://orcid.org/0000-0001-6353-0170
Xing Lu https://orcid.org/0000-0003-2619-9305
Steve Mairs https://orcid.org/0000-0002-6956-0730
Masafumi Matsumura https://orcid.org/0000-0002-6906-0103
Gerald Moriarty-Schieven https://orcid.org/0000-0002-0393-7822
Nguyen Bich Ngoc https://orcid.org/0000-0002-5913-5554
Nagayoshi Ohashi https://orcid.org/0000-0003-0998-5064
Takashi Onaka https://orcid.org/0000-0002-8234-6747
Jonathan Rawlings https://orcid.org/0000-0001-5560-1303
Mark Rawlings https://orcid.org/0000-0002-6529-202X
Ekta Sharma https://orcid.org/0000-0002-4541-0607
Yoshito Shimajiri https://orcid.org/0000-0001-9368-3143
Mehrnoosh Tahani https://orcid.org/0000-0001-8749-1436
Motohide Tamura https://orcid.org/0000-0002-6510-0681
Xindi Tang https://orcid.org/0000-0002-4154-4309
Kohji Tomisaka https://orcid.org/0000-0003-2726-0892
Le Ngoc Tram https://orcid.org/0000-0002-6488-8227
Hongchi Wang https://orcid.org/0000-0003-0746-7968
Jinjin Xie https://orcid.org/0000-0002-2738-146X
Hsi-Wei Yen https://orcid.org/0000-0003-1412-893X
Hyunju Yoo https://orcid.org/0000-0002-8578-1728
Hyeong-Sik Yun https://orcid.org/0000-0001-6842-1555
Yapeng Zhang https://orcid.org/0000-0002-5102-2096
Chuan-Peng Zhang https://orcid.org/0000-0002-4428-3183
Jianjun Zhou https://orcid.org/0000-0003-0356-818X
Sam Falle https://orcid.org/0000-0002-9829-0426
Frédérick Poidevin https://orcid.org/0000-0002-5391-5568
Jean-François Robitaille https://orcid.org/0000-0001-5079-8573

References

Andersson, B. G., Lazarian, A., & Vaillancourt, J. E. 2015, ARA&A, 53, 501
Andre, P., & Montmerle, T. 1994, ApJ, 420, 837
Arce, H. G., & Sargent, A. I. 2006, ApJ, 646, 1070
Arzoumanian, D., Furuya, R. S., Hasegawa, T., et al. 2021, A&A, 647, A78
Astropy Collaboration, Price-Whelan, A. M., Sipőcz, B. M., et al. 2018, AJ, 156, 123
Astropy Collaboration, Robitaille, T. P., Tollerud, E. J., et al. 2013, A&A, 558, A33
Bailer-Jones, C. A. L., Rybizki, J., Fouesneau, M., Mantelet, G., & Andrae, R. 2018, AJ, 156, 58
Beckwith, S. V. W., Sargent, A. I., Chini, R. S., & Guesten, R. 1990, AJ, 99, 924
Bence, S., Padman, R., Isaak, K., Wiedner, M., & Wright, G. 1998, MNRAS, 299, 965
Bonnor, W. B. 1956, MNRAS, 116, 351
Caselli, P., Benson, P. J., Myers, P. C., & Tafalla, M. 2002, ApJ, 572, 238
Chandrasekhar, S., & Fermi, E. 1953, ApJ, 118, 116
Chapin, E. L., Berry, D. S., Gibb, A. G., et al. 2013, MNRAS, 430, 2545
Chen, J.-H., Evans, N. J., Lee, J.-E., & Bourke, T. L. 2009, ApJ, 705, 1160
Cohen, M. 1980, AJ, 85, 29
Coudé, S., Bastien, P., Kirk, H., et al. 2016, MNRAS, 457, 2139
Crutcher, R. M. 2004, Ap&SS, 292, 225
Crutcher, R. M., Nutter, D. J., Ward-Thompson, D., & Kirk, J. M. 2004, ApJ, 600, 279
Currie, M. J., & Berry, D. S. 2014, KAPPA: Kernel Applications Package, Astrophysics Source Code Library, ascl:1403.022
Currie, M. J., Berry, D. S., Jenness, T., et al. 2014, in ASP Conf. Ser. 485, Starlink Software in 2013, ed. N. Manset & P. Forshay (San Francisco, CA: ASP), 391
Davis, L. 1951, PhRv, 81, 890
de Geus, E. J., Bronfman, L., & Thaddeus, P. 1990, A&A, 231, 137
Dempsey, J. T., Friberg, P., Jenness, T., et al. 2013, MNRAS, 430, 2534
Drabek, E., Hatchell, J., Friberg, P., et al. 2012, MNRAS, 426, 23
Ebert, R. 1955, ZA, 37, 217
Federrath, C. 2015, MNRAS, 450, 4035
Fehér, O., Tóth, L. V., Kraus, A., et al. 2022, ApJS, 258, 17
Friberg, P., Bastien, P., Berry, D., et al. 2016, Proc. SPIE, 9914, 991403
Gaia Collaboration, Brown, A. G. A., Vallenari, A., et al. 2021, A&A, 649, A1
Garufi, A., Dominik, C., Ginski, C., et al. 2022, A&A, 658, A137
Goldreich, P., & Kylafis, N. D. 1981, ApJL, 243, L75
Goldreich, P., & Kylafis, N. D. 1982, ApJ, 253, 606
Heiles, C., & Troland, T. H. 2005, ApJ, 624, 773
Hennebelle, P., & Inutsuka, S.-i 2019, FrASS, 6, 5
Herbst, W., & Warner, J. W. 1981, AJ, 86, 885
Hildebrand, R. H. 1983, QJRAS, 24, 267
Hildebrand, R. H., Kirby, L., Dotson, J. L., Houde, M., & Vaillancourt, J. E. 2009, ApJ, 696, 567
Hodapp, K.-W. 1994, ApJS, 94, 615
Holland, W. S., Bintley, D., Chapin, E. L., et al. 2013, MNRAS, 430, 2513
Hull, C. L. H., Girart, J. M., Tychoniec, Ł., et al. 2017, ApJ, 847, 92
Hull, C. L. H., Gouellec, V. J. M. L., Girart, J. M., Tobin, J. J., & Bourke, T. L. 2020, ApJ, 892, 152
Hwang, J., Pattle, K., Parsons, H., Go, M., & Kim, J. 2023, AJ, 165, 198
Jijina, J., Myers, P. C., & Adams, F. C. 1999, ApJS, 125, 161
Karoly, J., Soam, A., Andersson, B. G., et al. 2020, ApJ, 900, 181
Kim, G., Tatematsu, K., Liu, T., et al. 2020, ApJS, 249, 33
Kirchschlager, F., Bertrang, G. H. M., & Flock, M. 2019, MNRAS, 488, 1211
Kirk, H., Hatchell, J., Johnstone, D., et al. 2018, ApJS, 238, 8
Krumholz, M. R., & Federrath, C. 2019, FrASS, 6, 7
Kwon, W., Pattle, K., Sadavoy, S., et al. 2022, ApJ, 926, 163
Lazarian, A., & Hoang, T. 2007, MNRAS, 378, 910
Lee, C.-F., & Ho, P. T. P. 2005, ApJ, 624, 841
Lee, C.-F., Mundy, L. G., Stone, J. M., & Ostriker, E. C. 2002, ApJ, 576, 294
Liu, J., Qiu, K., Berry, D., et al. 2019, ApJ, 877, 43
Liu, J., Zhang, Q., & Qiu, K. 2022, FrASS, 9, 943556
Loinard, L., Torres, R. M., Mioduszewski, A. J., & Rodríguez, L. F. 2008, ApJL, 675, L29
Loren, R. B. 1989, ApJ, 338, 902
Lyo, A. R., Kim, J., Sadavoy, S., et al. 2021, ApJ, 918, 85
Mairs, S., Dempsey, J. T., Bell, G. S., et al. 2021, AJ, 162, 191
Mairs, S., Johnstone, D., Kirk, H., et al. 2015, MNRAS, 454, 2557
Mathieu, R. D., Benson, P. J., Fuller, G. A., Myers, P. C., & Schild, R. E. 1988, ApJ, 330, 385
Matthews, B. C., McPhee, C. A., Fissel, L. M., & Curran, R. L. 2009, ApJS, 182, 143
Moriarty-Schieven, G. H., Johnstone, D., Bally, J., & Jenness, T. 2006, ApJ, 645, 357
Myers, P. C. 2017, ApJ, 838, 10
Myers, P. C., Heyer, M., Snell, R. L., & Goldsmith, P. F. 1988, ApJ, 324, 907
Nakano, T., & Nakamura, T. 1978, PASJ, 30, 671
Ostriker, E. C., Stone, J. M., & Gammie, C. F. 2001, ApJ, 546, 980
Parsons, H., Dempsey, J. T., Thomas, H. S., et al. 2018, ApJS, 234, 22
Pattle, K., Fissel, L., Tahani, M., Liu, T., & Ntormousi, E. 2022a, arXiv:2203.11179

Pattle, K., Lai, S.-P., Di Francesco, J., et al. 2021, ApJ, 907, 88
Pattle, K., Lai, S.-P., Hasegawa, T., et al. 2019, ApJ, 880, 27
Pattle, K., Lai, S.-P., Sadavoy, S., et al. 2022b, MNRAS, 515, 1026
Pattle, K., Ward-Thompson, D., Berry, D., et al. 2017, ApJ, 846, 122
Pattle, K., Ward-Thompson, D., Kirk, J. M., et al. 2015, MNRAS, 450, 1094
Planck Collaboration, Ade, P. A. R., Aghanim, N., et al. 2016a, A&A, 586, A138
Planck Collaboration, Ade, P. A. R., Aghanim, N., et al. 2016b, A&A, 586, A132
Planck Collaboration, Ade, P. A. R., Aghanim, N., et al. 2016c, A&A, 594, A28
Pontoppidan, K. M., Salyk, C., Blake, G. A., & Käufl, H. U. 2010, ApJL, 722, L173
Roy, A., André, P., Palmeirim, P., et al. 2014, A&A, 562, A138
Sadavoy, S. I., Di Francesco, J., Johnstone, D., et al. 2013, ApJ, 767, 126
Schnee, S., Enoch, M., Noriega-Crespo, A., et al. 2010, ApJ, 708, 127
Shirley, Y. L., Nordhaus, M. K., Grcevich, J. M., et al. 2005, ApJ, 632, 982
Soam, A., Pattle, K., Ward-Thompson, D., et al. 2018, ApJ, 861, 65
Soler, J. D., Hennebelle, P., Martin, P. G., et al. 2013, ApJ, 774, 128
Wardle, J. F. C., & Kronberg, P. P. 1974, ApJ, 194, 249
Ward-Thompson, D., Di Francesco, J., Hatchell, J., et al. 2007, PASP, 119, 855
Ward-Thompson, D., Karoly, J., Pattle, K., et al. 2023, ApJ, 946, 62
Ward-Thompson, D., Kirk, J. M., Crutcher, R. M., et al. 2000, ApJL, 537, L135
Ward-Thompson, D., Pattle, K., Bastien, P., et al. 2017, ApJ, 842, 66
Ward-Thompson, D., & Whitworth, A. P. 2011, An Introduction to Star Formation (Cambridge: Cambridge Univ. Press)
Weintraub, D. A., Tegler, S. C., Kastner, J. H., & Rettig, T. 1994, ApJ, 423, 674
Yang, Y.-L., Green, J. D., Evans, N. J. I., et al. 2018, ApJ, 860, 174
Yen, H.-W., Koch, P. M., Hull, C. L. H., et al. 2021, ApJ, 907, 33
Yoon, S.-Y., Lee, J.-E., Lee, S., et al. 2021, ApJ, 919, 116
Young, C. H., Bourke, T. L., Young, K. E., et al. 2006, AJ, 132, 1998